POLITECNICO DI TORINO

Master's degree in aerospace engineering

Master of Science Thesis

THERMAL ANALYSIS AND INTEGRATION OF LIQUID COOLING GARMENTS FOR ANALOG SPACESUITS: VALIDATION IN THE LUNA FACILITY

Supervisors:

Professor Nicole Viola

Juergen Schlutz

Candidate:

Roberta Carini

July 2026

Abstract

Amid the enthusiasm surrounding the Artemis missions and the widespread pride in this new era of human space exploration, humanity is venturing into unprecedented frontiers. In this context, careful ground segment preparation and extensive crew training are of utmost importance, and high-fidelity simulations have never been more critical to ensure mission success.

This thesis presents a novel approach to the use of Life Support Systems, focusing on cooling systems, in an analog environment, the LUNA Analog facility, and discusses the associated challenges, particularly those arising from the higher gravity compared to the Moon. A key challenge is the potential displacement of the cooling system pipes caused by the harness of the analog Spacesuit. The weight of the water bladder also presents a practical issue, which could be mitigated in future tests with the Gravity Offloading System, potentially allowing the use of two bladders simultaneously.

The cooling system, composed of a pump, interconnected pipes, and a water bladder, was integrated into an analog suit designed to replicate the movement constraints of NASA's spacesuits. This integration required targeted modifications to the suit, including redesigned CAD models of the Portable Life Support System (PLSS) to ensure optimal fit and functionality.

A series of experiments was conducted in the LUNA testbed using custom-built sensor setup for temperature, pressure, flow, and humidity, alongside thermal imaging, to evaluate both the system's relevance for EVA activities and its operational efficiency. The study also examined potential modifications to improve performance and enhance the interface between the suit and the life support system, thereby improving usability and realism.

Alongside experimental testing, computational fluid dynamics (CFD) simulations were used to study fluid behaviour within the pipes, which cannot be directly observed when the system is enclosed in the Suit. By combining sensor data with CFD results, a more complete understanding of both fluid dynamics and heat transfer processes was achieved, providing detailed visualization of system performance.

Additionally, metabolic rate estimation based on oxygen consumption and carbon dioxide production was explored as a key parameter for real-time cooling control, supporting the development of future AI-driven thermal regulation systems.

The results demonstrate the thermodynamic criticalities of LCG systems under simulated EVA conditions, revealing that localized pressure points can severely degrade regional cooling efficiency dropping it down to just 29% of its nominal baseline capacity. However, the fluidic network safely tolerates uniform conduit deformations up to 2 mm without significant performance loss, and the integration of protective TPU supports proves capable of completely mitigating these localized occlusions. Ultimately, these findings provide valuable insights into the operational experience and physical challenges faced by astronauts during EVA activities, supporting the design and optimization of future life support systems for lunar missions.

Table of Contents

List of Figures

List of Tables

Acronyms

ISRU	In Situ Resource Utilisation
NASA	National Aeronautics and Space Administration
ESA	European Space Agency
JAXA	Japan Aerospace Exploration Agency
CSA	Canadian Space Agency
PSRs	Permanently Shadowed Regions
ISS	International Space Station
SLS	Space Launch System
LEO	Low Earth Orbit
EAC	European Astronaut Centre
DLR	German Aerospace Centre
FLEXHab	Future Lunar Exploration Habitat
EMU	Extravehicular Mobility Unit
xEMU	Exploration Extravehicular Mobility Unit
AxEMU	Axiom Extravehicular Mobility Unit
EV	Extravehicular
EVA	Extravehicular Activity
LCG	Liquid Cooling Garments
LCVG	Liquid Cooling and Ventilation Garments
CFD	Computational Fluid Dynamics
TPU	Thermoplastic Polyurethane
CAD	Computer Aided Design
PLSS	Portable Life Support System
MLI	Multi-Layer Insulation
TMG	Thermal Micrometeoroid Garment
HUT	Hard Upper Torso
LTA	Lower Torso Assembly
DCM	Display and Control Module
SCU	Service Centre Unit
EXCON	Exploration Concept of Operations
PPE	Personal Protective Equipment
PCM	Phase Change Materials
RTD	Resistance Temperature Detector
PTC	Positive Temperature Coefficient
ADC	Analog to Digital Converter
PCB	Printed Circuit Board
GPIO	General Purpose Input/Output
FSR	Force Sensitive Resistors
RH	Relative Humidity
ASIC	Application-Specific Integrated Circuit
IMU	Inertial Measurement Unit
COTS	Component Off The Shelf
CHT	Conjugate Heat Transfer

HPC	High-Performance Computing
REE	Rate of Energy Expenditure
ODE	Ordinary Differential Equations
PID	Proportional Integral Derivative
MPC	Model Predictive Control

1 Introduction

1.1 Human exploration and Artemis program

Human Exploration has never been as important as in these years in which our interest is moving towards new and further boarders than Earth's orbits. The moon is the first step towards future rich of discoveries and management and development of new extraterrestrial habitat and technologies.

The lunar exploration would allow the human species to learn and experience new techniques to survive in critique and challenging environments through ISRU (In Situ Resource Utilisation), adaptive and recycling capabilities, cooperation between different interested actors.

In this scenario, Artemis missions are essential to set a milestone in the human exploration: the **Artemis program** is a human spaceflight project of NASA in collaboration with international partners such as the European, Japanese, and Canadian space agencies (ESA , JAXA , and CSA). The program's goal is to land astronauts on the Moon for the first time since Apollo 17 , including the first woman. The plan is to subsequently conduct human lunar landings annually. In reference to the Apollo program, it was named after Artemis , the moon goddess and twin sister of Apollo in Greek mythology [1].

The first Artemis moon landing was originally planned for 2024, but due to delays in the provision of a lunar module and new spacesuits, it cannot take place before 2028.

Unlike the Apollo era's 'flags and footprints' approach, Artemis focuses on **sustainable exploration** regions: a key differentiator of the Artemis program is its focus on the **Lunar South Pole** [1,2]. This region is of immense strategic value due to the presence of **Permanently Shadowed Regions (PSRs)**, which are believed to contain significant deposits of water ice. Harvesting this ice is critical not only for life support (drinking water and oxygen) but also for producing liquid hydrogen and oxygen to be used as rocket propellant, effectively turning the Moon into a 'gas station' for the solar system [1]. Central to the program's long-term viability is the **Lunar Gateway**, an international outpost orbiting the Moon. Unlike the International Space Station (ISS) which orbits Earth, the Gateway will serve as a multi-purpose docking hub, staging point for lunar surface landings, and a laboratory for deep-space research [2,3]. It will allow for more flexible mission profiles and serve as a critical communication relay between the Moon's surface and Earth.

Beyond exploration, the Artemis program serves as a rigorous testing ground for **autonomous systems and robotics**. The harsh lunar environment—characterized by abrasive regolith, extreme temperature fluctuations (from -170°C to 120°C), and high radiation—requires the development of highly resilient materials and advanced AI-driven navigation. The data gathered from these missions will provide invaluable insights into human physiology during long-duration spaceflight, informing the protocols for the first human journey to Mars.

Figure 1 *Earthset from lunar orbit. Source: NASA*

Missions

Artemis I

Launched in 2022, Artemis I was the first in a series of increasingly complex missions that will enable human exploration at the Moon and future missions to Mars. Artemis I was the first integrated flight test of NASA's Deep Space Exploration Systems: the Orion spacecraft, Space Launch System (SLS) rocket, with the upgraded Exploration Ground Systems at Kennedy Space Centre in Cape Canaveral, Florida [1].

Artemis II

The first crewed Artemis flight marks a key step toward long-term return to the Moon and future missions to Mars. The successful completion of the Artemis II mission in April 2026 provided the definitive flight-test data required to certify the Orion spacecraft for deep-space operations [1,3]. By achieving a lunar flyby with a four-person crew and conducting complex proximity manoeuvres, the mission bridged the gap between automated testing and the human-centric exploration of the lunar South Pole planned for the late 2020s. The architecture of human spaceflight is evolving to meet the demands of **deep-space environments**. Beyond the protective shield of Low Earth Orbit (LEO), missions face unprecedented challenges in radiation shielding, autonomous life-support systems, and communication latency [1]. Artemis II represents the critical bridge in this evolution, testing the resilience of human-rated spacecraft in the proving ground of cislunar space, where the margin for error is significantly narrower than in previous orbital missions.

Artemis III

The Artemis III mission will launch crew in the Orion spacecraft on top of the SLS (Space Launch System) rocket to test rendezvous and docking capabilities between Orion and commercial spacecraft needed to land astronauts on the Moon. NASA will announce specifics on the Artemis III mission design and crew closer to the 2027 launch [1].

Artemis IV

NASA continues to target early 2028 for the first Artemis lunar landing, a date that has remained unchanged since mid-2025. After reaching lunar orbit, the crew will transfer from Orion to a commercial lunar lander for their descent to the Moon's surface [1,2].

Artemis V

Using the standard SLS (Space Launch System) rocket configuration, NASA expects to launch this lunar surface mission by late 2028, with subsequent missions planned roughly once per year [1,2].

1.2 LUNA Analog Facility

Within the framework of next-generation crewed spaceflight, the European Astronaut Centre (EAC) and the German Aerospace Centre (DLR) in Cologne, Germany, are establishing high-fidelity terrestrial baselines for future lunar surface operations through advanced analog simulation campaigns [4].

The LUNA Analog Facility is a state-of-the-art joint venture managed by ESA and DLR, designed to serve as an integrated testbed for complex human-machine-environment interactions. The core infrastructure consists of a large-scale, hall-type enclosure housing an artificial lunar regolith testbed.

To replicate the physical and morphological terrain of the lunar surface, the testbed utilizes **EAC-1**, a volcanic regolith simulant sourced from the Eifel region [6]. While the terrestrial environment prevents a perfect match to true lunar dust in terms of low-gravity particle volatility and extreme micro-abrasiveness, EAC-1 provides a highly realistic mineralogical and chemical facsimile.

Because the simulant distribution includes a high concentration of inhalable particulate matter smaller than $200\,\mu$m, stringent occupational safety protocols mandate the use of full-body protective garments and ocular filtration systems for all personnel inside the main hall. To systematically investigate the destructive, abrasive mechanics of lunar dust on extravehicular hardware, the facility integrates an isolated lunar dust chamber dedicated to studying dust charging phenomena and active mitigation technologies [4,6].

Focus Area	Core Activities & Technologies Tested
Geosciences & Exploration	Geological and seismic regolith characterization; terrestrial rock mapping using basaltic samples from Norway and Greenland; laser spectroscopy.
In-Situ Engineering	In-Situ Resource Utilization (ISRU) technologies; automated drilling and lunar mining methodologies.
Robotics & Operations	Telerobotics; human-rover co-exploration; standardized communication protocols mirroring ISS and real-world EVA workflows.

Table 1 *Operational Capability Matrix: The LUNA testbed bridges the gap between hardware prototyping and operational readiness by supporting concurrent research across multiple disciplines.*

Adjacent to the primary simulation hall is the **Future Lunar EXploration Habitat (FLEXHab)**, a modular human-in-the-loop habitat designed to support up to four crew members [4]. Future infrastructural iterations will establish a hermetic, contiguous connection between FLEXHab and the LUNA hall via a dedicated corridor and airlock system. This architectural upgrade will enable seamless, uninterrupted shirtsleeve-to-vacuum transition profiles during long-duration analog isolation missions.

To mimic the challenging lighting topography of the lunar south pole, the facility integrates a dynamic sun simulator. This subsystem generates low-angle, high-contrast artificial solar illumination, casting realistic, sharp shadows across the artificial craters and boulders distributed throughout the testbed.

Planned structural upgrades include a robotic **gravity offloading system**. Suspended from rail-guided overhead gantries on the ceiling, this computer-controlled tether network will actively counteract $5/6ths$ of the gravity vector, reducing the effective weight of rovers, instruments, and suited astronauts to match the true gravitational acceleration of the Moon (1.62 m/s^2) [4,5].

Analog Spacesuit Integration and Human-in-the-Loop Testing

Critical components of LUNA's operational evaluation framework are the Analog **Spacesuits**. These ensembles are biomechanically engineered to impose the exact kinematic constraints and limited range of motion characteristic of flight-certified extravehicular mobility units, specifically referencing the Axiom Extravehicular Mobility Unit (AxEMU) architecture [4,6].

These suits are systematically utilized by astronauts, LUNA team members, and industrial partners during integrated field trials. A primary use case includes the ergonomic validation of the LUNA tool cart, engineered to transport geology kits, core drills, and regolith sample containment systems.

By conducting iterative testing loops with suited operators, researchers can capture high-fidelity extravehicular feedback, allowing for the optimization of standardized operational procedures, metabolic heat profiles, and ergonomic hardware baselines in a highly controlled environment [4,5].

Figure 2 *Moon-testbed inside LUNA. Credit: ESA/DLR*

1.3 Research gap and motivation

In this scenario, the cooling system plays an important role for the comfort and feeling of the astronaut even if only within the simulation in the analogue environment. It gives the EV (Extravehicular, the person inside the Spacesuit) the sense of cool and a reliable body temperature distribution he would feel during real operations.

Despite the critical role of Liquid Cooling Garments (LCGs) in Extravehicular Activities (EVA), a significant **research gap** exists in the effects of the integration of a LCG inside the Spacesuit simulator, with physiological monitoring and performance evaluation within analog environments.

Specifically, current analog spacesuit's cooling system research lacks:

1. **The Physical-Gravity Trade-off:** Quantitative data on how the suit's harness and structural weight induce pipe deformation and flow resistance in a 1g environment. This mechanical interference, specific to terrestrial simulations, directly degrades the cooling efficiency required for high-fidelity training.
2. **The Indirect Calorimetry Framework:** A robust methodology for implementing **indirect calorimetry** (O_2 consumption and CO_2 production monitoring) *inside* an analog suit to characterize the astronaut's real-time metabolic heat load.

Currently, most analog simulations rely on static or manual cooling settings. This thesis addresses this gap by demonstrating that **indirect calorimetry** can be successfully utilized within the LUNA Facility to map metabolic rates. By validating this data-driven approach alongside CFD and mechanical optimizations (such as TPU supports), this work provides the essential physiological baseline required to develop future **AI-driven, autonomous thermal regulation systems**.

1.4 Thesis objectives and methodology

The primary objective of this research is to enhance the thermal management and operational fidelity of analog extravehicular activities (EVAs) within the LUNA Analog Facility. To achieve this, the study adopts a multidisciplinary methodology that bridges mechanical engineering, computational fluid dynamics (CFD), and human physiology.

First, the research focuses on architectural integration, involving the physical modification of an analog spacesuit. This phase required the redesign of Portable Life Support System (PLSS) components through CAD modeling to accommodate the cooling system's hardware—comprising a pump, a water bladder, and a network of pipes—ensuring that the suit's mobility and ergonomic constraints were preserved.

A core methodological pillar of this thesis is the Experimental-CFD Correlation. By deploying a custom-built sensor suite (measuring temperature, pressure, flow, and humidity), experimental data were collected during testbed sessions. These data were then used to validate CFD simulations, providing a detailed visualization of fluid behavior and heat transfer in areas where direct observation was impossible due to the suit's enclosure. This correlation is crucial for assessing cooling coherence and identifying temperature gradients across different body segments, particularly under the mechanical stress of the suit's harness.

Furthermore, the study explores the transition from manual to autonomous thermal regulation. The methodology introduces indirect calorimetry as a key diagnostic tool, monitoring oxygen consumption O2 and carbon dioxide production CO2 to estimate real-time metabolic heat. This physiological characterization serves as the foundational data layer for developing future AI-driven algorithms capable of governing the cooling system based on the astronaut's actual metabolic demand.

Finally, the research evaluates the system's efficiency by quantifying performance losses due to gravity-induced pipe deformation. By integrating these experimental and computational results, the thesis provides a comprehensive validation of LCG systems for lunar analog environments, supporting the optimization of life support architectures for the Artemis era.

2 State of the Art

2.1 Spacesuits for planetary exploration

Space suits represent one of the most complex human-support systems developed for space exploration. Modern Extravehicular Activity (EVA) suits are not simply protective garments, but integrated miniature spacecraft capable of providing atmospheric pressure, oxygen supply, thermal regulation, radiation protection, communication systems, and mobility support in the hostile environment of space [7].

The suits used during the Apollo missions, particularly the Apollo A7L Suit, were the first systems specifically designed for planetary exploration. Unlike previous Mercury and Gemini suits, which were mainly conceived for intravehicular operations or short-duration EVAs, the Apollo suits had to support extended activities on the lunar surface, including walking, geological sampling, and rover operations. The A7L architecture introduced important innovations such as the Portable Life Support System (PLSS), multilayer thermal insulation, micrometeoroid protection, and articulated joints to improve astronaut mobility on the Moon [8] . However, despite these advancements, Apollo suits remained relatively stiff and mobility was still significantly constrained by the internal gas pressurization.

The current NASA EVA suit, known as the Extravehicular Mobility Unit (EMU), was developed primarily for microgravity operations aboard the Space Shuttle and the International Space Station (ISS). The EMU is a modular system composed of interchangeable components that allow adaptation to astronauts with different anthropometric characteristics. Compared to Apollo suits, the EMU provides improved life support, greater operational duration, enhanced safety systems, and long-term reusability [7,9]. Nevertheless, the EMU was not designed for planetary locomotion. Its architecture is optimized for zero-gravity operations, where astronauts move using handrails rather than walking. Consequently, lower body mobility is limited, and the suit is not suitable for lunar or Martian surface exploration.

A typical EVA space suit consists of multiple specialized layers, each designed to perform specific protective and operational functions. Although the architecture varies depending on the mission profile and generation of the suit, most modern EVA suits share a multilayer configuration developed to ensure astronaut survival in the extreme space environment. Starting from the innermost section, astronauts wear a Liquid Cooling and Ventilation Garment (LCVG), responsible for removing metabolic heat and controlling humidity through a network of water-circulating tubes [10]. Above the LCVG, the pressure bladder layer maintains the internal suit pressure necessary for human survival in vacuum conditions. This layer is generally made of flexible gas-retaining materials and works together with the restraint layer, which prevents excessive expansion of the suit under pressurization and helps preserve its structural shape [9].

The outer portions of the suit include several thermal and protective layers. Multilayer insulation (MLI), composed of alternating reflective and insulating materials, minimizes heat transfer caused by solar radiation and extreme temperature fluctuations. Additional layers provide protection against micrometeoroids, abrasion, and lunar dust contamination. In Apollo suits, the outer Thermal Micrometeoroid Garment (TMG) was primarily composed of Beta cloth, a Teflon-coated fiberglass material selected for its thermal resistance and fireproof properties [8]. Modern EMU and Artemis-generation suits employ more advanced composite fabrics and improved joint architectures to increase durability, flexibility, and resistance to abrasive planetary regolith [11].

In addition to the fabric layers, EVA suits integrate rigid structural components such as the Hard Upper Torso (HUT), helmet assembly, gloves, bearings, and mobility joints. These components are essential for maintaining pressure integrity while allowing astronaut mobility [9]. The Portable Life Support System (PLSS), mounted on the back of the suit, supplies oxygen, removes carbon dioxide, regulates temperature, and powers communication and monitoring systems [10]. Together, these layers and subsystems transform the EVA suit into an autonomous human-support spacecraft capable of operating in the hostile conditions of planetary and orbital environments.

For the Artemis program, NASA and Axiom Space are developing the next generation of planetary EVA suits based on the xEMU (Exploration Extravehicular Mobility Unit) architecture. These new systems, commonly referred to as AxEMU suits, aim to overcome the limitations of both Apollo and ISS-era suits [11]. The Artemis suits are specifically designed for lunar surface exploration in the challenging environment of the lunar South Pole. Compared to the EMU, the new suits provide significantly improved lower torso mobility, allowing astronauts to walk, crouch, kneel, and collect geological samples more naturally. In addition, Artemis suits integrate advanced dust mitigation technologies, modular components, rear-entry architectures, and enhanced anthropometric inclusivity [12]. These developments reflect the transition from survival-oriented systems toward highly integrated human-performance platforms optimized for long-duration planetary exploration.

2.2 Thermal Control Systems in Space Suits

Thermal control represents one of the most critical subsystems in EVA suit engineering. In space and on planetary surfaces, astronauts are exposed to extreme thermal environments characterized by the absence of atmospheric convection, intense solar radiation, and large temperature variations. Temperature ranges can vary from -170°C to 120°C. Space suits must therefore maintain the astronaut's body temperature within safe physiological limits while simultaneously dissipating the metabolic heat generated during physical activity [10].

During the Apollo missions, thermal regulation was achieved through a combination of passive and active systems. The Apollo A7L suits incorporated multilayer insulation to minimize external heat transfer and protect astronauts from thermal radiation. Additionally, astronauts wore a Liquid Cooling Garment underneath the pressure suit to remove excess metabolic heat [8]. Although highly innovative for its time, the Apollo thermal control system had limited adaptability and was constrained by the relatively short duration of lunar EVAs. Lunar dust contamination also posed a significant challenge, reducing the effectiveness of thermal surfaces and degrading suit materials over time.

Modern EMU suits currently used on the ISS employ more advanced thermal regulation systems. The EMU integrates active cooling loops, ventilation circuits, water sublimators, and thermal insulation layers capable of supporting long-duration EVAs in low Earth orbit [9]. The Primary Life Support System continuously circulates oxygen and cooling water while removing carbon dioxide and humidity from the suit environment. Compared to Apollo systems, EMU thermal control provides greater reliability, redundancy, and operational autonomy. However, these systems were designed primarily for microgravity conditions and not for dusty planetary environments.

The Artemis-generation suits introduce substantial improvements in thermal control technology. Future lunar missions will involve longer EVAs in extreme thermal conditions near permanently shadowed regions at the lunar South Pole. Consequently, the AxEMU thermal control system incorporates more efficient heat rejection technologies, improved insulation materials, advanced ventilation systems, and enhanced resistance to lunar dust contamination [11,13]. The integration of new thermal management architectures is essential not only for astronaut survival but also for maintaining mobility, comfort, and operational performance during extended planetary exploration activities.

During Extravehicular Activities (EVAs), astronauts can produce significant amounts of metabolic heat due to physical exertion associated with locomotion, sample collection, maintenance operations, and manipulation of tools. In the vacuum of space, heat cannot be dissipated through natural convection as on Earth. Consequently, EVA suits rely on dedicated thermal control systems capable of actively removing excess heat and maintaining thermal equilibrium [10].

The thermal control system of a modern EVA suit can be divided into three main subsystems:

- Thermal insulation layers;
- Active heat removal systems;
- Ventilation and humidity control systems [9].

The external layers of the suit provide passive thermal protection against solar radiation, extreme temperatures, and micrometeoroids. Multilayer insulation (MLI) is typically composed of alternating reflective and insulating materials that minimize radiative heat transfer. These layers reduce both heat absorption from solar radiation and heat loss toward the surrounding environment.

However, passive insulation alone is insufficient to remove the metabolic heat generated by the astronaut. For this reason, EVA suits employ active thermal regulation systems based on liquid cooling technologies. The astronaut wears a Liquid Cooling and Ventilation Garment (LCVG) underneath the pressure garment [14]. The LCVG contains a network of small flexible tubes through which cooled water circulates continuously.

The operating principle of the thermal control system is based on heat exchange between the astronaut's body and the circulating cooling fluid. Metabolic heat produced by the astronaut is transferred to the water flowing through the LCVG tubing. The warmed water is then transported to the Portable Life Support System (PLSS), where the excess heat is rejected into space through dedicated heat rejection devices [10].

In the Apollo A7L suits, thermal regulation was achieved using a sublimator-based cooling system. Water exposed to the vacuum environment partially sublimated, absorbing heat from the circulating cooling loop and lowering the water temperature before recirculation to the astronaut. Although highly effective, sublimators consume water and are sensitive to contamination.

The current Extravehicular Mobility Unit (EMU) used aboard the International Space Station employs a similar thermal control architecture but with improved reliability, redundancy, and cooling performance

The next-generation Artemis suits, based on the xEMU/AxEMU architecture, introduce further improvements in thermal management. Future lunar missions will involve extended EVA operations in the challenging thermal environment of the lunar South Pole, characterized by extreme temperature gradients. Consequently, Artemis thermal control systems are designed to provide enhanced cooling efficiency, improved dust resistance, higher operational autonomy, and better thermal adaptability to variable workloads [11,13].

In addition to heat removal, the ventilation subsystem plays a fundamental role in maintaining astronaut comfort and safety. Oxygen circulation inside the suit removes carbon dioxide, humidity, and excess heat generated by respiration and perspiration. Airflow also prevents visor fogging and helps maintain uniform thermal conditions within the suit.

The main components of a typical EVA thermal control system are illustrated in Table 2.

Component	**Function**
Liquid Cooling and Ventilation Garment (LCVG)	Removes metabolic heat from the astronaut body
Cooling water loop	Transfers absorbed heat to the PLSS
Portable Life Support System (PLSS)	Manages cooling, ventilation, oxygen supply, and CO_2 removal
Sublimator / heat rejection device	Rejects heat into space
Ventilation circuit	Removes humidity and distributes oxygen
Multilayer insulation	Protects against external thermal environment

Table 2 *EVA TCS components*

The operating principle of the liquid transport loop, Figure 3, works as follows:

1. The LCVG (Liquid Cooling and Ventilation Garment)

The heart of the system is the LCVG 107 (top left). This is a form-fitting undergarment worn by the astronaut, interlaced with miles of plastic tubing.

- Heat Absorption: Water flows through these tubes in contact with the body, absorbing metabolic heat.
- Flow: The now-warmed water exits the LCVG and travels toward the cooling system.

2. Temperature Control (DCM and Cooling Control Valve)

The astronaut can manually adjust their comfort level using the Cooling Control Valve 321, located on the DCM 300 (the control panel on the chest).

- W (Warm): The valve diverts water away from the sublimator, causing warm water to recirculate.
- C (Cold): The valve directs water toward the sublimator for maximum cooling.

3. The Pump and Separator (123C and 128L)

A pump (123C) is required to circulate the liquid through the loop.

- Gas Trap (128L): Before re-entering the circuit, the water passes through a separator. This removes any air bubbles that could block the pump or reduce system efficiency.

4. The Sublimator (Sublimator 140)

This acts as the suit's "radiator," but it operates using a unique process called sublimation.

- Feedwater Loop: Since there is no air in space to cool a traditional radiator, the system uses the Feedwater Loop (the dashed blue line).
- The Process: Water from the supply tank reaches the sublimator and freezes upon contact with a porous plate exposed to the vacuum of space.
- Heat Rejection: Heat from the warm water in the cooling loop causes this ice to sublimate (turn directly from a solid to a gas).
- Evaporative Cooling: The resulting water vapor escapes into the vacuum, carrying away thermal energy.

5. SCU (Service Center Unit) Connector

In the bottom left of Figure 3 is the SCU. This is the umbilical that connects the suit to the spacecraft or space station before the astronaut begins the EVA (Extravehicular Activity).

- Pre-cooling: During this phase, the suit receives chilled water directly from the ship's systems to preserve the suit's internal water reserves and ice.

Summary of the Cycle

- Absorption: Water warms up against the astronaut's skin (LCVG).
- Transport: The pump moves the warm water toward the backpack (PLSS).
- Regulation: The control valve determines how much water needs to be cooled.
- Thermal Discharge: The sublimator expels heat into the vacuum of space.
- Return: The now-chilled water returns to the LCVG to start the cycle again.

The system uses a closed loop for the coolant (pink) but an open "expendable" loop for the feedwater (blue). This is why spacewalks are limited in duration by the amount of water available for the sublimator.

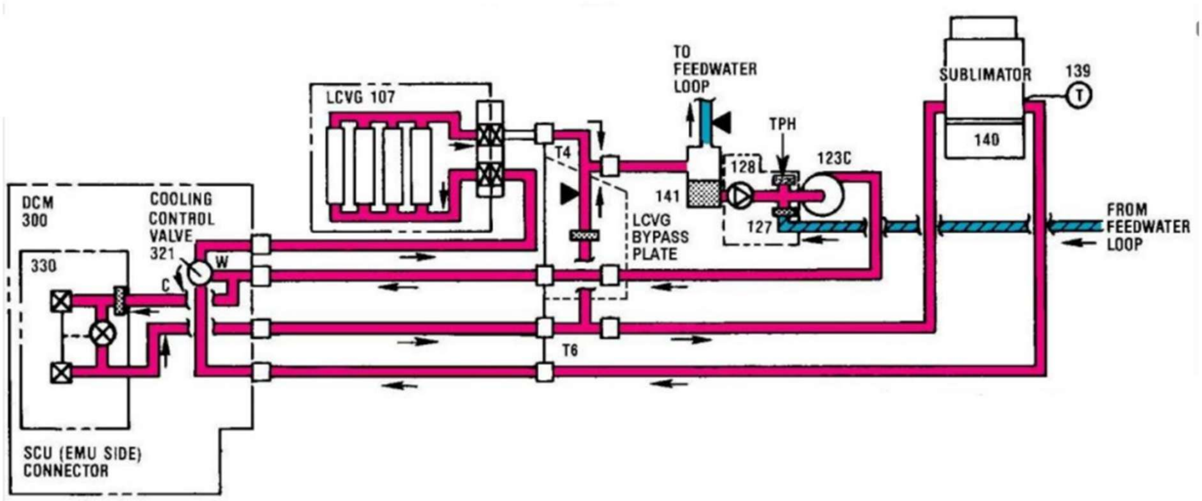

Figure 3 *Liquid transport loop. Source: NASA EMU Databook, 2017*

Artemis-generation suits further extend these capabilities by integrating advanced materials, improved thermal architectures, and enhanced resistance to lunar dust contamination. These developments reflect the increasing importance of thermal management systems in enabling long-duration planetary exploration missions.

2.3 Liquid Cooling and Ventilation Garments (LCVG)

The Liquid Cooling and Ventilation Garment (LCVG) is a fundamental component of EVA suits and plays a crucial role in astronaut thermal regulation. Since the human body continuously generates metabolic heat during physical activity, especially during EVA operations, passive insulation alone is insufficient to maintain thermal equilibrium. The LCVG addresses this issue by circulating cooled water through a network of small tubes distributed across the astronaut's body. Simultaneously, ventilation systems remove humidity and carbon dioxide from the suit interior.

In aerospace and EVA (Extravehicular Activity) systems, the liquid cooling garment is often described as part of a broader **garment assembly** rather than as a single cooling layer. In NASA-style spacesuit architecture, the assembly is divided into several integrated subsystems that work together to provide thermal regulation, ventilation, structural stability, and fluid distribution. The **LCVG Restraint Assembly** is the structural layer that keeps the cooling tubes and fabric closely fitted to the astronaut's body, preventing movement and ensuring efficient heat transfer. The **Liner Assembly** is the inner comfort layer worn against the skin, designed to improve comfort, moisture management, and hygienic separation between the body and the cooling network. The **Vent**

Plenum Assembly distributes ventilation airflow throughout the garment, helping remove humidity, carbon dioxide, and excess heat while supporting air circulation inside the suit. Finally, the **Multiple Water Connector** is the interface that connects the garment's internal tubing network to the spacecraft or Portable Life Support System (PLSS), allowing chilled water to circulate into and out of the garment. Together, these elements form a complete wearable thermal-management system.

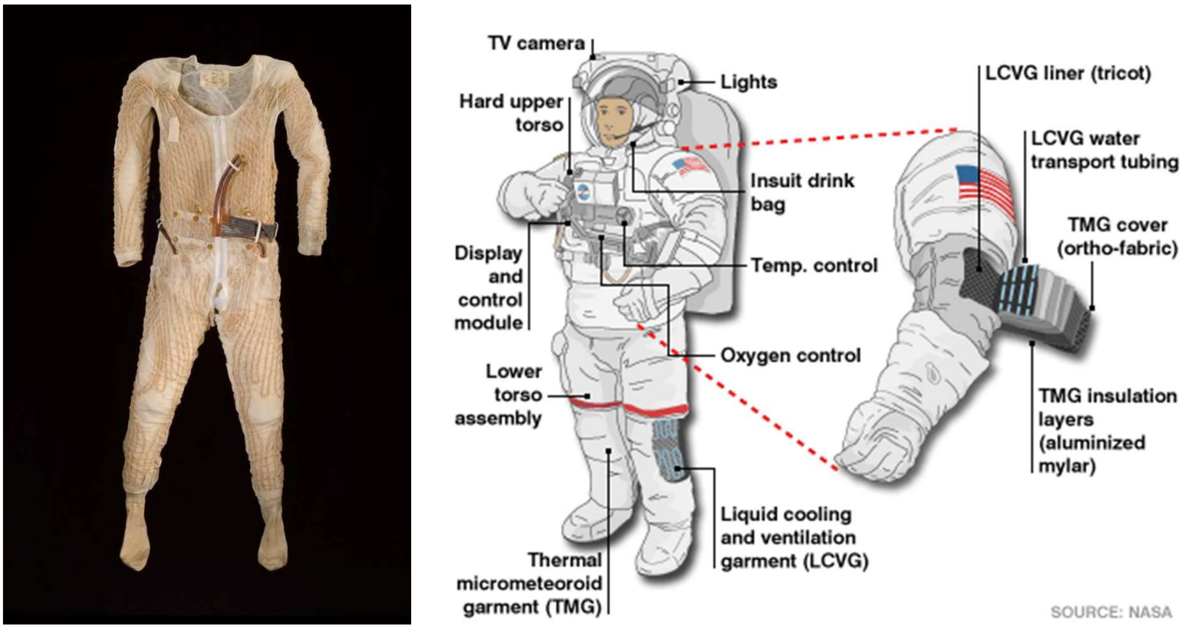

Figure 4 *Apollo LCVG and a fully fitted Spacesuit representation. Source: NASA*

The first operational implementation of liquid cooling technology was introduced in the Apollo A7L suits. This technology represented a major advancement compared to earlier Mercury and Gemini suits, where thermal regulation capabilities were considerably more limited. Nevertheless, Apollo LCVGs had relatively simple architectures and limited thermal adaptability.

In current EMU systems aboard the ISS, the Liquid Cooling and Ventilation Garment has evolved into a more sophisticated and reliable subsystem. Modern LCVGs provide continuous body cooling during EVAs that can last more than six hours. The garment covers most of the astronaut's body and integrates dense tubing networks that optimize heat removal efficiency. These improvements are necessary because modern ISS EVAs involve complex maintenance operations requiring prolonged physical effort.

Planetary EVAs require higher levels of mobility and involve more intense physical workloads than orbital operations. Consequently, future LCVGs are being designed to enhance thermal comfort while minimizing restrictions to astronaut movement. Current research focuses on lightweight tubing architectures, adaptive cooling systems, improved ventilation efficiency, and smart thermal management technologies capable of responding dynamically to astronaut metabolic activity. Compared to Apollo and current EMU systems, Artemis-generation LCVGs aim to provide greater thermal efficiency, improved comfort, and better integration with next-generation planetary EVA suit architectures [15].

LCG for terrestrial applications

Terrestrial personal cooling systems can be broadly categorized into passive, semi-passive, and active approaches depending on their energy requirements and heat rejection mechanisms. Passive systems include phase change material (PCM) garments and radiative cooling textiles, which rely on latent heat absorption or radiative heat loss to the environment; they are lightweight, silent, and intrinsically safe but offer limited cooling capacity and duration [16]. Semi-passive systems, such as evaporative cooling garments, enhance heat transfer through water evaporation and can provide effective short-term cooling in dry environments, though they are unsuitable for humid or contamination-sensitive settings. Active systems, primarily liquid cooling garments (LCGs) and thermoelectric wearables, use pumped fluid loops or solid-state heat pumps to actively transport heat away from the body; these systems offer the highest and most controllable cooling performance but require power supply, introduce mechanical complexity, and may present reliability or ergonomic constraints. Hybrid architectures that combine multiple mechanisms are increasingly common to balance efficiency, autonomy, and comfort. Within this landscape, compact liquid cooling systems designs emphasize reduced fluid volume, improved ergonomic integration, and enhanced compatibility with constrained environments such as EVA analog operations [17].

In Table 3 all those systems have been summed up considering the operational trade-offs within the frame of EVA simulations and integration in Suit simulator. The chosen architecture to better represent and simulate the real EVA LCG conditions is a water-cooling garment system, with pipes routing around the body.

Cooling system	Weight / bulk	Regolith contamination risk (H_2O / vapor)	EVA realism simulation fidelity	Operational duration	Integration in suit	Key advantages	Key limitations
Liquid Cooling Garment (LCG)	Medium–High	Medium–High (leak risk critical if H_2O loop exposed)	Very high	High (4–8+ h typical)	Well-established but bulky tubing routing	High heat removal capacity, proven NASA heritage	Leakage risk, tubing pinch points, complexity
Compact LCG	Medium	Low–Medium (reduced fluid volume → lower risk)	High–Very high	Medium–High (3–6+ h optimized)	Good (better ergonomics, reduced tubing volume)	Improved ergonomics, lower leak probability, better mobility	Requires advanced control, lower thermal buffer
PCM cooling vest (Phase Change Materials)	Medium–High	None	Medium (limited dynamic response)	Low (0.5–2 h typical)	Excellent (simple garment integration)	No fluids, intrinsically safe, silent	Limited cooling capacity, requires recharge infrastructure
Evaporative cooling garment	Low–Medium	High (water vapor + condensation + contamination risk in regolith environments)	Medium (poor under pressure suits)	Medium (2–4 h depending on conditions)	Moderate (humidity management issues)	Efficient in dry environments, low power	Incompatible with regolith + sealed EVA realism issues
Radiative cooling textiles (passive)	Very low	None	Low (ineffective under suit insulation)	High (passive)	Excellent (thin textile layer)	Zero energy, no fluids, no maintenance	Insufficient cooling power for EVA workloads
Thermoelectric (Peltier wearables)	High	None	Medium	Low–Medium (battery-limited)	Moderate–Poor (hot-side management issues)	Precise local control, no fluids	Very inefficient, heavy power demand, heat rejection problem
Hybrid systems (LCG + PCM / LCG + radiative layer)	Medium–High	Low–Medium (depends on liquid subsystem)	Very high	High	Complex but promising	Balanced performance, redundancy, adaptability	System complexity, integration challenges
Compact system (reference architecture)	Medium (optimized low volume loop)	Low (minimal fluid inventory reduces catastrophic leak risk)	Very high (best compromise for analog EVA realism)	Medium–High	Good (ergonomic routing, reduced pinch points)	Best trade-off between mobility, safety, and thermal performance	Requires precise thermal control, less buffer than full LCG

Table 3 *Comparison of different ground-application LCGs [17]*

3 Analog Spacesuit System

3.1 Spacesuit Simulators Design

As mentioned in Section 1, one of the systems most frequently used within the facility is the spacesuit simulator: an unpressurized system developed by **Atlas Devices LLC**, an American company, to recreate the mechanical constraints experienced in the actual NASA xEMU spacesuit through the **EXCON (Exploration Concept of Operations) Suit** architecture [18]. Two spacesuits are currently available in the facility: an M-sized suit and an L-sized suit. The only difference between the two configurations is the shoulder width, which is larger in the L-sized version.

The spacesuit has several applications within the facility. It can be used for testing new equipment, conducting medical studies, supporting filming campaigns, or simply training users to experience the mechanical constraints and range of motion limitations of the joints and torso while operating inside the regolith testbed.

The suit is mounted on a dedicated rack structure, which keeps the spacesuit stable and easily manageable during safety inspections, preparation procedures, and donning and doffing operations. Access to the suit occurs through the rear opening, where the Portable Life Support System (PLSS) is attached after donning.

All procedures follow ISS standards, since the suit is not only used by LUNA team members but also by astronauts as part of their training activities [19].

The hardware configuration of the suit is composed of the following elements:

Hard Upper Torso (HUT)

The HUT includes the section of the suit extending from the waist upwards and comprises the torso structure, shoulder bearings, and arm bearings.

The shoulder bearings can rotate independently from the arm bearings. The arm and shoulder structures are mainly made of plastic components; in particular, the shoulder system consists of plastic rings capable of partially folding in order to accommodate movement. The rest of the torso structure includes both plastic and metallic components, the latter belonging to the main structural frame of the suit.

The metallic structure starts from the uppermost part of the suit with the so-called “bunny ears,” which are metallic hooks used to safely secure the suit to the rack.

The front section of the torso hosts the HUT Control Panel, which is easily reachable by the EV during EVA activities.

The panel is equipped with seven ON/OFF switches and can theoretically be connected to several subsystems, although it is currently not connected to any active hardware.

Lower Torso Assembly (LTA)

The Lower Torso Assembly includes the legs and hip bearings and represents the lower section of the suit. The operating principle of the lower joints is similar to that of the upper torso joints.

Helmet Assembly

The helmet assembly consists of the transparent helmet bubble with integrated lighting systems. The helmet is attached to the HUT through a dedicated locking mechanism.

Portable Life Support System (PLSS)

The Portable Life Support System consists of a plastic cover mounted onto a metallic frame plate and attached to the HUT through four external hinges with removable pins, two on each side.

Gloves and Boots

The gloves and boots are designed to resemble the real EVA hardware and allow users to walk inside the regolith hall and manipulate EVA tools during simulations.

It is important to note that the metallic components are designed to carry structural loads, whereas the plastic parts, are not intended for significant load-bearing applications.

Sizing brackets are mechanical elements that allow adjustment of the torso length according to the user's height. Five different bracket sizes are available, ranging from Size 0 (0 inches between the bottom of the HUT and the top of the waist bearing) to Size 4 (4 inches between the bottom of the HUT and the top of the waist bearing).

Figure 5 *EXCON Analog Suits. Source: DLR*

The entire structure is covered with fabric garments designed to resemble the external covers of the real xEMU spacesuit. Each garment section is attached to the others using high-strength Velcro.

3.2 Suit Team

The suit team plays a fundamental role during all suit operations, since the EV cannot wear the entire spacesuit system independently.

Only trained personnel are authorized to handle the suit.

Suit technicians are responsible for performing donning and doffing procedures, assisting the EV while entering the suit, and connecting all the required interfaces. They also carry out suit preparation and fitting procedures, including safety inspections to verify that all systems are functioning correctly and that no dangerous components or pressure points are present for the EV.

During fitting procedures, suit technicians may also replace mechanical components such as sizing brackets.

For every simulation activity, suit technicians must accompany the EV inside the testbed and remain nearby while carrying the emergency extrication kit. They must be ready to intervene immediately in the event of emergencies or suit malfunctions.

In emergency scenarios—such as EV distress, acute pain, or loss of consciousness—an emergency extrication procedure is executed. In these situations, the suit technicians, supported by the Safety Officer, use the specialized tools contained in the emergency kit to rapidly disassemble key parts of the suit and extract the EV safely [20].

To operate inside the regolith testbed without introducing external contaminants or risking personal exposure, suit technicians must wear specific Personal Protective Equipment (PPE) assemblies:

- PPE suit;
- Rubber boots;
- Ventilation system;
- Gloves.

This equipment prevents contamination of the regolith environment while simultaneously protecting the operators from regolith exposure. Suit technicians must be formally qualified and certified for this role.

The Procedure Coordinator is responsible for reading and supervising all procedures, verifying that every operation is performed correctly, and monitoring the EV for possible signs of discomfort or anomalies.

The Suit Safety Officer is responsible for all suit-related safety aspects during procedure execution. In emergency situations, the Suit Safety Officer leads the emergency response procedures. Their presence is mandatory during all operations involving an EV.

Whenever campaigns involving EVA simulations are organized, a dedicated Campaign Team is selected to prepare and execute the campaign according to the process described in the LUNA Analog Facility Concept of Operations document.

During simulations, the EV is required to report their status to the team every 30 minutes. If the conditions are judged unacceptable, the EV must immediately return to the stand.

3.3 Ergonomics and Human Factors

Since the suit structure itself is relatively heavy, ergonomics and wearer comfort represent critical aspects that must be prioritized during operations.

3.3.1 Interface with the EV

In order to wear the suit, a dedicated harness system is required.

Before donning, the EV wears a waist belt consisting of a wide and tightly fitting soft belt equipped with two small hooks on the sides.

Attached to the suit, at waist height, there are two straps that must first pass through the openings of the waist belt once the EV is inside the suit. The straps are then routed through two additional openings located on the hips of the structure and finally tightened using dedicated cinches, securing the first two attachment points.

At chest level, two shoulder straps are attached to the HUT. These straps pass over the shoulders and connect to two cinches positioned on the rear section of the HUT, where they are tightened by the suit technicians.

Overall, the EV is connected to the suit through four attachment points:

- two shoulder attachment points using the shoulder straps and rear cinches;
- two waist attachment points using one strap on each side routed through the waist belt.

The ideal weight distribution should be approximately 60% on the waist and 40% on the shoulders.

If, after donning, the EV reports discomfort or if most of the suit weight is concentrated on the shoulders, the distribution can be adjusted through the front shoulder strap attachment points. Using a wrench, the bolt located below the front panel can be regulated in order to redistribute the load, either relieving the shoulders or reducing the load applied to the waist.

3.3.2 Ventilation

Although the suit is not fully sealed and includes openings to the external environment, ventilation is still required whenever the helmet is worn.

Inside the PLSS, mounted onto the metallic plate, an air filter is installed with an airflow rate set to approximately 205 L/min.

An airflow diverter is mounted on the upper section of the PLSS in order to distribute the airflow throughout the helmet.

The air filter is essential for protecting the EV from regolith exposure by filtering the air before it enters the helmet. The filter type is the same as the one used by the rest of the team and by external users entering the regolith hall while wearing PPE.

The ventilation system is activated by the suit technicians during the donning procedure before entering the hall.

3.3.3 Padding

An important ergonomic aspect is the comfort of the EV inside the suit. At the same time, it is also necessary for the EV to remain properly constrained within the suit in order to realistically reproduce movement sensations and prevent shifts in the centre of gravity.

To avoid impacts between the EV and the rigid or pinching components of the HUT, and to prevent injuries during movement, padding elements are installed inside the suit.

The standard configuration generally consists of a front cushion designed to compress and stabilize the body. The chest area represents the most critical region requiring protection.

A dedicated testing campaign was conducted to identify and evaluate the main pressure points inside the suit.

During the tests, the EV was asked to assume different positions, including:

- facing downward;
- facing upward;
- sideways positions.

Particular attention was dedicated to evaluating the distance between the chin and the helmet ring, since this interface could potentially represent a hazardous contact point.

Following the testing activity, several padding configurations were developed, as shown in Table 4.

The optimal configuration may vary depending on the user's body size, body shape, and comfort requirements.

Configuration	***Description***	***Picture***
F1	Front 1 Thinner cushion combined with padding stripes on the lower ring	
F2	Front 2 Large cushion positioned low enough to avoid pressure on the EV’s throat. If the cushion does not cover the lower ring, a stripe of padding needs to be added	
PLSS1	Full Configuration PLSS equipped with two side stripes and one stripe on the lower part. This configuration is most likely to be used with thinner front padding	
PLSS 2	Partial Configuration PLSS equipped with a single stripe on the lower part.	
PLSS 3	No Padding PLSS without any back padding. This option is typically preferred for larger users or when thicker front padding is installed.	

B	Back Foam stripe on the metallic section of the lower back area.	
S	Shoulders Padding positioned below the shoulder straps and on the upper circumference of the shoulder bearings	 

Table 4 *Padding configurations*

4 Cooling system

4.1 Architecture

The cooling system integrated within the facility, as previously outlined, is a specialized liquid cooling garment (LCG) developed by **COMPCOOLER** [21]. This specific ground-application system was selected from the architectural trade-offs evaluated in Table 3 due to the following engineering and operational drivers:

- **Optimized Weight Profile:** The subsystem mass remains within acceptable limits for a terrestrial operator;
- **Extended Mission Profile:** It allows for a substantial increase in the continuous duration of simulation activities;
- **Ergonomic Integration:** The compact design features a tight-fitting vest, facilitating seamless integration inside the rigid spacesuit shell;
- **High Simulation Fidelity:** Its operation closely resembles the underlying layout and body-interface principles of actual flight-qualified systems used in space exploration.

The architecture of the system, shown in the Figure 6, is composed as follows: a battery 7.4 V 2200mAh powers a water pump, controlled by a 3-levels manual controller: high 400ml/min, medium 300 ml/min and low 200 ml/min, a 5 litres bladder to store the liquid, and the cooling vest, made of nylon fabric and integrating 6 mm diameter silicone pipes routed throughout the garment, specifically 2 inlet and outlet pipes for the upper body and 2 for the lower.

The four pipes merge into a larger manifold pipe on the inlet side, and the same configuration is used on the outlet side.

Figure 6 *Liquid Cooling Garment in LUNA*

The system can be used in two different configurations (Figure 7):

- Single bladder configuration, up to 3 hours of autonomy
  The connections are arranged as follows:
  - Pump inlet connected to the bladder outlet
  - Pump outlet connected to the cooling vest inlet
  - Cooling vest outlet connected to the bladder inlet

- Dual-bladder configuration, up to 8 hours of autonomy
  The connections are arranged as follows:
  - Outlets of both bladders connected to the pump inlet
  - Pump outlet connected to the cooling vest inlet
  - Cooling vest outlet connected to the inlets of both bladders

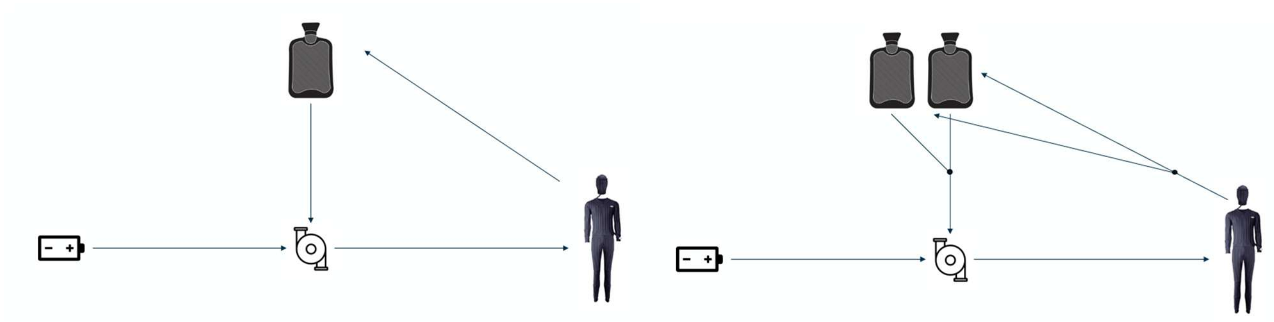

Figure 7 *Single vs Dual bladder configuration*

Currently, only the first configuration is used in the facility, since the weight of the two bladders, 10 litres in total, would not be sustainable for the astronaut inside the suit. In the future, with the implementation of the Gravity Offloading System, which will relieve the subject of approximately 5/6ths of their body weight, the dual-bladder configuration could be used to increase the mission duration.

4.2 Ground vs space environment

An analog environment differs significantly from a real space environment in several key aspects that directly affect the design and operation of cooling systems used in spacesuits.

In a true space or lunar EVA context, such as operations performed with NASA's Extravehicular Mobility Unit (EMU), thermal regulation is extremely challenging because heat rejection occurs primarily in vacuum conditions where convection is absent and radiation and phase-change processes dominate. For this reason, real space suits rely on systems such as liquid cooling and ventilation garments combined with sublimators, where water is intentionally frozen and then sublimated in vacuum to remove large amounts of metabolic heat.

However, in a lunar analog facility on Earth, these same physical principles cannot be replicated. The presence of an atmosphere makes sublimation-based cooling unusable, not only because there is no vacuum to drive the phase change efficiently, but also because releasing water vapor would contaminate the test environment, alter humidity levels, and interfere with regolith simulants and experimental conditions.

Similarly, one might also consider evaporative cooling as a potential alternative in analog EVA environments, since in principle it exploits the phase change of water from liquid to vapor to absorb significant amounts of heat, conceptually resembling the sublimation-based cooling used in real space systems [9]. However, in practice it is not used in lunar analog facilities or ground-based spacesuit tests. The main reason is that evaporative cooling introduces uncontrolled moisture into the environment, which would significantly increase ambient humidity and fundamentally alter the physical properties of the testbed. This is especially problematic in facilities using regolith simulants, where moisture can change cohesion, adhesion, electrostatic behavior, and dust transport characteristics, leading to non-representative results. Additionally, evaporation in a closed or semiclosed laboratory environment is difficult to regulate precisely, making thermal performance unstable and dependent on local environmental conditions rather than controlled system parameters. It can also interfere with sensors, optical systems, and experimental instrumentation designed to operate in dry or vacuum-like conditions. For these reasons, although evaporative cooling might seem like a conceptually space-relevant approach, it is ultimately unsuitable for analog EVA testing environments.

As a result, unlike space systems where the thermal control loop is effectively “open” in the sense that heat can be rejected to the environment through phase change into vacuum, the cooling system used in the facility is fully closed loop thermally and operationally. It continuously recirculates and removes heat without any mass loss to the environment. This fundamental difference means that analog cooling systems are inherently simpler, more maintainable, and less constrained by mass, power, and reliability requirements compared to flight systems, but at the same time they cannot faithfully reproduce the extreme thermal boundary conditions experienced in real extraterrestrial EVA operations.

Another fundamental difference between space environments and analog EVA facilities is gravity, which has a major impact on both human performance and thermal system behavior. In a real lunar environment, gravity is approximately one-sixth of Earth’s gravity, meaning that body weight, fluid distribution, and mechanical loads on the suit are significantly reduced. This affects not only astronaut locomotion and metabolic expenditure, but also the behaviour of cooling systems inside the suit, particularly liquid loops, where reduced hydrostatic pressure and altered buoyancy can influence flow stability, bubble formation, and two-phase interactions. In contrast, terrestrial analog facilities operate under full Earth gravity, which introduces higher mechanical loads on the user and can increase metabolic heat production due to greater effort required for movement, especially when using exoskeletons with harnesses. At the same time, gravity-driven effects on fluids, such as natural stratification and drainage, behave very differently compared to lunar conditions, making it impossible to fully replicate the thermal-fluid dynamics of EVA cooling systems. As a result, while analog environments can approximate workload and operational procedures, they cannot accurately reproduce the coupled effects of reduced gravity on both human physiology and thermal control performance.
The harness issue due to gravity is one of the most concerning regarding the integration of cooling system inside the analogue spacesuit: as previously mentioned, harness is needed to wear the spacesuit system. The piece of harness that limits the most the performance of the cooling is the waistbelt: because it must be tight, it can easily occlude the pipes, and the effect is even amplified by the weight of the suit. For this reason, a study has been conducted on the deformation of the pipes.

Despite these limitations, analog cooling systems are still designed to provide the astronaut with a thermal sensation that is as close as possible to what would be experienced in space, maintaining stable skin temperature regulation, perceived comfort levels, and realistic heat removal rates at the suit interface. In this way, even if the underlying fluid dynamics and gravitational effects cannot be fully replicated, the system can still effectively reproduce the subjective thermal experience of EVA operations and support realistic human-in-the-loop testing of procedures and workloads.

4.3 Motivation

The cooling system plays a crucial role not only in actual Extra-Vehicular Activity (EVA) operations, but also in analogue missions and simulation environments. Although the thermal and metabolic loads in these contexts are generally lower than those experienced in real space conditions, EVA simulations can still lead to significant metabolic heat production. This, in turn, may result in fatigue, profuse sweating, and an overall increase in body temperature.

During a campaign activity aimed at testing internally developed EVA tools, the chest temperature of the EV was monitored using a Movesense sensor while the subject wore a spacesuit simulator. The tools were arranged on a cart that had to be transported and operated within the testbed environment. The tasks included pushing the cart over a considerable distance, bending repeatedly to test different tools, and walking extensively along the facility corridors. Overall, the activity represented a physically demanding EVA-like scenario.

The external (chest) temperature of the subject inside the suit increased from an initial value of approximately 34 °C to about 38 °C after 30 minutes of activity. This rise in temperature was consistent with the physiological condition reported by the EV, who experienced high levels of fatigue and workload. Visible signs of thermal strain, such as excessive sweating, were also observed.

These results highlight that comfort and thermal regulation during EVA simulations are essential factors for maintaining performance and preventing the onset of hyperthermia conditions. Effective thermal management is therefore not only relevant for real EVA missions, but also for ensuring realistic, safe, and sustainable analogue testing environments.

4.4 Sensors system

For the EV in general, but used specifically when the cooling was worn to monitor the fluctuations of the external skin temperature, a sensor system was designed and developed, using the following sensors:

- Temperature probes PT1000, analogic
- Pressure sensor, analogic
- Gas monitoring sensor, *sens66*

4.4.1 Solid-State Physics of PT1000 RTD Sensors

The temperature measurement subsystem relies on a PT1000 Resistance Temperature Detector (RTD). The underlying physical principle governing this sensor is the temperature dependence of electrical resistivity in high-purity metals—specifically Platinum (Pt) [22]. Inside a metallic conductor, electrical conduction is driven by free electrons moving through a crystalline lattice. As the temperature of the metal increases, thermal energy induces high-amplitude lattice vibrations, known in solid-state physics as **phonons**.

These localized vibrations increase the scattering cross-section for conduction electrons, reducing their mean free path and macroscopically manifesting as an increase in electrical resistance. This behavior defines a Positive Temperature Coefficient (PTC). The nomenclature "PT1000" refers to the sensor material (Platinum) and its nominal reference resistance (R_0) of exactly $1000\ \Omega$ at $0\ ^{\circ}\mathrm{C}$. For the standard industrial operating range ($0\ ^{\circ}\mathrm{C}$ to $100\ ^{\circ}\mathrm{C}$), this relationship is highly linear and mathematically modeled by the simplified Callendar-Van Dusen equation [23]:

$$R(T) = R_0(1 + \alpha T)$$

Where $R_0 = 1000\ \Omega$, T is the temperature in Celsius, and α is the temperature coefficient of resistance, typically equal to $0.00385\ ^{\circ}\mathrm{C}^{-1}$ according to the DIN EN 60751 standard. Consequently, a temperature shift of 1 ˚C yields a minor resistance variation of only $\Delta R \approx 3.85\ \Omega$.

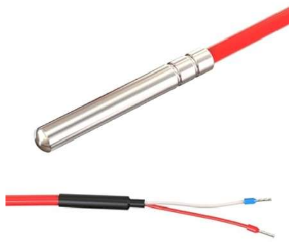

Figure 8 *PT1000 sensor*

Signal Conditioning via Wheatstone Bridge Configuration

Due to the exceptionally small magnitude of ΔR per degree Celsius, standard voltage divider topologies are inadequate. A simple voltage divider yields an output signal riding on a large DC offset voltage, meaning a high-resolution Analog-to-Digital Converter (ADC) would waste most of its dynamic range digitizing a static voltage rather than the temperature-induced variations. To overcome this limitation, a **Wheatstone Bridge** circuit was implemented on the custom PCB.

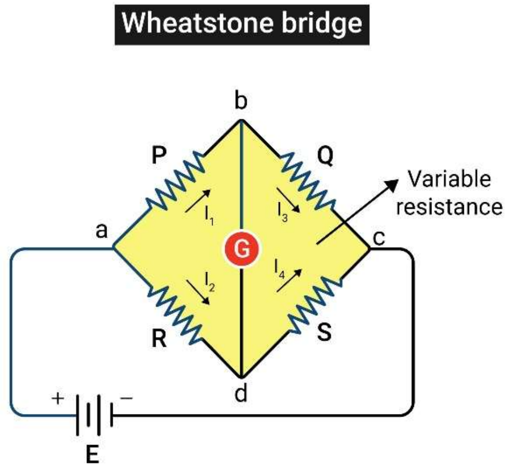

***Figure 9** Theoretical diagram of a Wheatstone bridge topology. Source: Jonas Reuel*

As illustrated in the schematic topology, the bridge splits a single voltage source (V_{CC}) into two parallel resistive rami. In this design, three arms consist of high-precision, low-temperature-drift fixed resistors ($R_1, R_2, R_3 = 1000\ \Omega$, matching the nominal R_0 of the sensor), while the fourth arm is the PT1000 RTD (R_{RTD}).

The differential output voltage (ΔV) is sampled across the central nodes of the two rami ($V_b - V_d$). The transfer function of the bridge is defined as:

$$\Delta V = V_{CC} \cdot \left(\frac{R_{RTD}}{R_1 + R_{RTD}} - \frac{R_3}{R_2 + R_3} \right)$$

When the system is at 0 °C, $R_{RTD} = R_1 = R_2 = R_3 = 1000\ \Omega$. Substituting these values into the equation yields $\Delta V = 0$ V. The bridge is perfectly balanced. This differential implementation provides two fundamental engineering advantages [24]:

1. **Null-Method Precision:** Eliminating the base $1000\ \Omega$ offset allows the system to map the entire dynamic input range of the ADC exclusively to the temperature-induced voltage variations (ΔV).
2. **Common-Mode Rejection Ratio (CMRR):** High-frequency noise or voltage fluctuations originating from the V_{CC} power supply rail affects both rami symmetrically. Because the ADC evaluates the difference ($V_b - V_d$), this common-mode noise is mathematically and physically canceled out, drastically lowering the signal-to-noise ratio (SNR) of the frontend.

Additionally, current flowing through the PT1000 causes power dissipation via Joule heating ($P = I^2 \cdot R$), a phenomenon known as **self-heating**. To prevent this dissipated thermal energy from artificially raising the sensor's temperature and corrupting the environment data, the excitation voltage V_{CC} and the bridge resistors were engineered to restrict the sensor current well below 1 mA.

Custom PCB Design and Hardware Interfacing

To maintain absolute signal integrity, eliminate parasitic resistances, and guarantee rugged mechanical stability, a custom Printed Circuit Board (PCB) was developed. Standard breadboard prototyping introduces variable contact resistances and stray capacitances that easily degrade micro-volt differential signals. By deploying a dedicated PCB, all discrete components—including the precision bridge resistors, decoupling capacitors, and the ADC IC—were permanently secured via lead-free solder alloy.

The physical architecture of the hardware stack is partitioned as follows:

Sensor-to-PCB Analog Connections

The PT1000 sensors are routed to the PCB using a dedicated layout. The terminal leads of the RTD are soldered directly onto through-hole pads or high-quality screw terminals on the PCB. This physical soldering minimizes contact impedance, which is critical since even a small $0.38\ \Omega$ parasitic resistance from a loose wire connection would introduce a systematic measurement error of roughly $+0.1\ ^{\circ}\text{C}$.

Analog-to-Digital Conversion (ADC)

The central nodes of the Wheatstone Bridge are routed through short, symmetric, differential PCB traces to the differential input pins (AIN_0, AIN_1) of an external high-resolution ADC (16-bit ADS1115). An external ADC is strictly mandatory for this architecture because **the Raspberry Pi 5 does not incorporate any native analog-to-digital hardware channels** on its GPIO header. The ADC samples the analog differential voltage ΔV, quantizes it into a discrete digital bitstream, and filters out high-frequency electromagnetic interference (EMI).

PCB-to-Raspberry Pi 5 Mechanical and Digital Interface

The custom PCB was designed as an expansion shield or "HAT" topology that mechanically mounts directly on top of the Raspberry Pi 5 using its standard 40-pin GPIO (General Purpose Input/Output) header strip.

The physical and logical connection mapping between the PCB components and the Raspberry Pi 5 pins is structured through the following hardware buses:

PCB Component Terminal	**Raspberry Pi 5 GPIO Pin**	**Signal Type / Function**
VCC (Bridge & ADC Power)	Pin 2 or 4 (5V) or Pin 1 (3.3V)	DC Power Supply Rail

PCB Component Terminal	Raspberry Pi 5 GPIO Pin	Signal Type / Function
GND	Pin 6, 9, 14, 20, 25, 30, 34, or 39	System Common Ground Reference
SDA (Serial Data)	Pin 3 (GPIO 2)	I^2C Bi-directional Data Bus
SCL (Serial Clock)	Pin 5 (GPIO 3)	I^2C Clock Synchronizing Signal

Table 5 *PCB-Raspberry Pi connection mapping*

Evolutionary Design Iterations and Field-Testing Challenges

In the initial proof-of-concept phase, the system was assembled using a solderless breadboard connected directly to the Raspberry Pi 5 GPIO header via loose jumper wires. Without a Wheatstone bridge conditioning network, the preliminary design accommodated six temperature sensors via simple voltage dividers. However, this layout proved highly unreliable; the absence of differential noise cancellation and the presence of stray capacitances caused severe signal oscillations, compromising data integrity.

This breadboard configuration was field-tested during an early operational campaign involving the suit's liquid cooling system. Due to the lack of soldered connections, the hardware was highly vulnerable to mechanical stress. During the donning procedures of the suit, the lack of wire routing structure and insufficient cable length forced the team to temporarily secure the entire Raspberry Pi and breadboard assembly to the side of the Portable Life Support System (PLSS) using Velcro. This severely degraded the structural robustness of the system; during the simulation, mechanical movements caused several critical wires to detach, resulting in an immediate loss of connection and data dropouts.

To rectify these structural flaws, the custom PCB was developed, mandating a technical trade-off. Implementing the Wheatstone bridge architecture significantly increased the required circuit footprint. Due to the strict **PCB space and form-factor constraints** imposed by the integration volume within the PLSS, the maximum number of supported temperature probes had to be reduced from six to four. Ultimately, four waterproof PT1000 probes were selected and attached to the EV body using medical-grade adhesive tape to monitor skin/body temperature.

The environment inside the space suit simulator required significant modifications to the sensor cabling layout. While the native cables attached to the PT1000 probes measured 1 meter in length, this was insufficient to route the wires from the subject's body extremities to the processing core housed inside the PLSS. To resolve this, custom extension cables were spliced and permanently hand-soldered to each probe, achieving a total routing length of approximately 3 meters per sensor.

Physically, the selected probes feature a rugged, waterproof encapsulation, making them theoretically suitable for immersion and real-time thermal monitoring of the liquid cooling bladder. However, because the cooling bladder must be hermetically sealed prior to each suit deployment, introducing a physical cabling harness through the bladder wall was deemed inadequate and mechanically high-risk for the current version of the suit integration.

Right before a subsequent testing campaign, a system malfunction was detected during general checks, manifesting as a complete signal loss on one of the four temperature channels. A systematic debugging and troubleshooting diagnostic were performed on the hardware stack. The root cause was isolated to a cold solder joint (an imperfect solder connection) along one of the extension cable junctions. The high resistance of the faulty joint disrupted the impedance balance of the respective Wheatstone bridge arm. Once a precise re-soldering procedure was performed to establish a flawless molecular and electrical bond, the channel's signal integrity was fully restored, validating the system for the testing campaign.

4.4.2 Pressure sensor and application

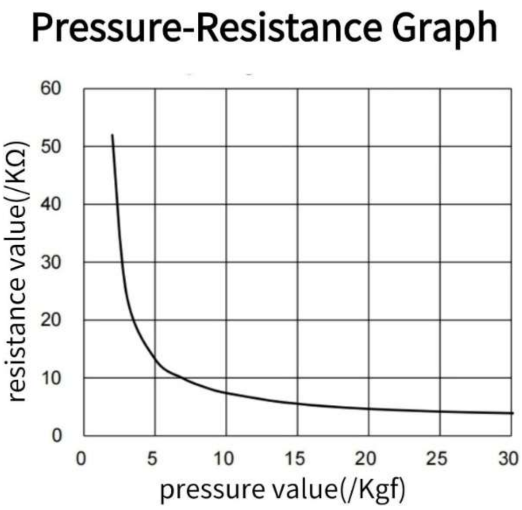

Figure 10 *Pressure-Resistance graph*

In addition to temperature monitoring, the developed hardware integrates a thin-film resistive pressure sensor to capture mechanical interactions. The device utilized is a Force Sensitive Resistor (FSR), a polymer thick-film (PTF) sensor whose electrical resistance decreases non-linearly as an increasing normal force is applied to its active surface [25].

The physical mechanism driving the FSR is not based on the strain of a single bulk conductor (like a classic metal strain gauge), but rather on **piezoresistive surface micro-contacts** and percolation theory.

The sensor is constructed of two thin, flexible polymer substrate layers separated by a microscopic air gap maintained by a peripheral spacer adhesive [26]:

1. **The Upper Layer:** Coated with a semi-conductive, carbon-based piezoresistive ink featuring microscopic surface asperities (rough protrusions).
2. **The Lower Layer:** Patterned with two sets of interdigitating, independent conductive metal fingers routed to the two external terminals.

When no force is applied, the air gap keeps the layers separated, acting as an open circuit with an unloaded residual resistance greater than $10\ \text{M}\Omega$. When a force (F) hits the active area, the upper polymer deforms, forcing the microscopic protrusions of the semi-conductive ink to physically bridge (shunt) the interdigitating fingers underneath.

At low forces, only the tallest microscopic protrusions establish electrical contact. As the mechanical force escalates, the macro-surface flattens, increasing the microscopic contact surface area and establishing an exponential number of parallel electrical pathways. According to Ohm's Law, this sudden boom of parallel conduction paths drastically drops the overall equivalent resistance (R_{FSR}).

Once the initial mechanical elasticity of the substrate is overcome—a point known as the **"break force"** or turn-on threshold (typically around 20 g to 100 g)—the resistance drops drastically from tens of mega-ohms down to approximately $10\ \text{k}\Omega$. Beyond this threshold, the FSR enters its active dynamic zone, where its resistance is inversely proportional to the applied force, following an inverse power-law characteristic before hitting saturation at high forces:

$$R_{FSR} \propto \frac{1}{F}$$

Unlike the PT1000, which requires a highly precise Wheatstone Bridge due to its tiny ΔR, the FSR undergoes a massive resistance swing across several orders of magnitude (from $> 10\ \text{M}\Omega$ down to $\sim 100\ \Omega$). Because this signal swing is so large, a standard **voltage divider** circuit is perfectly adequate and prevents circuit over-complication on the PCB.

The FSR is placed in series with a high-precision static pull-down resistor (R_M, $10\ \text{k}\Omega$ to balance sensitivity), forming a divider network fed by the PCB reference voltage V_{CC}:

$$V_{OUT} = V_{CC} \cdot \left(\frac{R_M}{R_{FSR} + R_M}\right)$$

As the force increases, R_{FSR} decreases toward zero, pushing the analog output voltage V_{OUT} asymptotically upward toward V_{CC}.

This analog voltage node (V_{OUT}) is routed directly to a dedicated single-ended input channel of the same external ADC on the PCB. The converted digital data is then pulled by the Raspberry Pi 5 via the I2C/SPI bus alongside the temperature data, allowing the system to sync thermal and mechanical metrics in real time.

The primary operational application of this force-sensitive resistor was to monitor and quantify the mechanical deformation of the liquid cooling pipes when subjected to compressive forces exerted by the suit's waistbelt. Because the flexible tubing runs underneath the heavy load-bearing structures of the suit, mechanical pinching represents a critical single-point failure mode that can severely mitigate or completely block the coolant circulation .

To establish a functional relationship between the sensor's electrical output and the actual physical state of the hardware, an empirical calibration campaign was executed. This procedure correlated the dynamic resistance shifts (ΔR_{FSR}) to the physically measured cross-sectional deformation of the pipe (measured in millimeters).

During fluid dynamics testing, it was observed experimentally that a pipe deformation threshold of **4 mm** induced a critical restriction in the tube's internal cross-section. Beyond this 4 mm boundary, the hydrodynamic flow resistance increased drastically, causing the mass flow rate of the cooling fluid to drop below acceptable operational parameters, thereby compromising the heat rejection capabilities of the cooling.

As previously noted, polymer-thick-film FSR sensors exhibit a significant nominal tolerance range of **5% to 25%**, making them inherently unsuitable for high-precision, continuous metrological measurements. However, by leveraging the empirical calibration data, the sensor was successfully utilized as a highly reliable **pressure threshold detector**. Instead of tracking continuous micro-variations of force, the system software was programmed to monitor the voltage divider output until it crossed the specific voltage threshold corresponding to the critical 4 mm mechanical deformation.

This implementation effectively transformed the analog sensor into an intelligent safety trigger, capable of immediately alerting the system when the waistbelt compression threatened the continuity of the liquid cooling loop.

Figure 11 *Force Sensitive Resistor*

4.4.3 Multi-Environmental Digital Sensing via Sensirion SEN66 Module

To extend the system's analytical capabilities beyond point-source temperature and localized mechanical force, a highly integrated environmental sensing node was introduced into the hardware architecture. The system deploys the Sensirion SEN66 multi-sensor module, an all-in-one digital platform engineered for comprehensive Air Quality (AQ) monitoring [27].

Unlike discrete analog components, the SEN66 abstracts complex physical transduction mechanisms internally, integrating a cluster of distinct sensors into a single, compact housing:

- **Particulate Matter (**$PM_{1.0}, PM_{2.5}, PM_{4.0}, PM_{10}$**)**: Operates on the physical principle of **laser scattering** (optical particle counting). An internal fan draws ambient air into a detection chamber where it intercepts a laser beam. The particles scatter the light, and a photodiode measures the scattering intensity and wave patterns. Internal microprocessors translate these optical pulses into mass concentration (μg/m^3) and particle count metrics.

- **Carbon Dioxide (CO_2):** Utilizes **Non-Dispersive Infrared (NDIR)** spectroscopy or photoacoustic sensing. It exploits the quantum mechanical property of gas molecules to absorb specific wavelengths of infrared light (specifically $4.26\ \mu$m for CO_2). The attenuation of light intensity traveling through the gas sample is directly proportional to the gas concentration, following the Beer-Lambert Law.
- **Volatile Organic Compounds (VOC) & Nitrogen Oxides (NO_x):** Rely on **Metal Oxide Semiconductor (MOS)** multi-pixel gas sensors. When gas molecules interact with the heated semiconductor surface (e.g., tin dioxide), chemical reduction or oxidation reactions alter the oxygen vacancy density in the crystal lattice, causing measurable shifts in electrical conductivity [28].
- **Relative Humidity and Temperature (RH/T):** Utilizes a capacitive relative humidity sensor, measuring capacitance changes between polymer-coated micro-electrodes as water vapor diffuses into the dielectric layer, alongside a bandgap digital temperature sensor.

Unlike the PT1000 and the FSR sensors, which require custom analog conditioning frontend circuitry routed through the custom PCB, the SEN66 abstracts all raw amplification and calibration internally via an integrated ASIC. To exploit this digital autonomy and eliminate any risk of electromagnetic interference (EMI) between high-speed digital lines and the delicate analog tracks, the system architecture completely segregates the data acquisition paths into two distinct physical domains:

1. **The Synchronous Bus Domain (Custom PCB):** Dedicated exclusively to routing, shielding, and digitizing the high-sensitivity analog signals from the PT1000 bridge and the FSR divider, communicating via the standard 40-pin GPIO header stack.
2. **The Plug-and-Play Peripheral Domain (Direct USB Connection):** Dedicated to the SEN66 module, which completely bypasses the custom PCB and interfaces directly with one of the native USB ports of the host computer.

Because the SEN66 handles all raw analog signal amplification, calibration, and environmental parameter computation internally via an integrated Application-Specific Integrated Circuit (ASIC), its hardware interface to Raspberry Pi is entirely digital.

Bus Interface to the Raspberry Pi 5

The SEN66 module is linked to the Raspberry Pi 5 via a specialized cable assembly that terminates on one end in a JST connector (mating with the sensor) and on the other in a standard **USB Type-A** connector plugged directly into the Raspberry Pi 5.

From an engineering perspective, this direct USB connection handles both electrical power delivery and logical data translation through the following mechanisms:

- **Integrated USB-to-UART Bridge:** Inside the USB connector casing (or along the cable assembly), a dedicated bridge integrated circuit is embedded. The SEN66 natively outputs its data using serial communication. The bridge chip acts as a hardware translator, converting the sensor's serial bitstream into differential USB data packets compliant with the USB protocol standard.
- **Plug-and-Play Driver Stack:** Upon connection, the Linux kernel running on the Raspberry Pi 5 automatically enumerates the USB device, loading the appropriate Virtual COM Port (VCP) driver. This creates a logical serial device node in the operating system filesystem allowing user-space software scripts to open a standard serial terminal connection at a specific baud rate to stream data.
- **Power Subsystem Isolation:** The SEN66 houses a mechanical air-sampling fan and an internal laser diode, which generate sharp current spikes during startup and continuous operation. Connecting the module directly via USB ensures that these transient power loads draw current directly from the Raspberry Pi's main power distribution rails. This keeps the voltage plane of the custom PCB extremely quiet, protecting the high-precision Wheatstone bridge from voltage sags that would degrade the accuracy of the PT1000 temperature readings.

Figure 12 *Sensirion sens66 module*

All these sensors were used to monitor EV's biomedical situation and represented an important tool for the study and testing activities described in the next subchapters.

4.5 Pipes integration within the Spacesuit

As illustrated in Figure 6, the liquid cooling conduits are integrated directly into the garment layout. The routing target specific anatomical regions where heat extraction is critical for core thermoregulation, with particular emphasis on the lower back and the anterior torso.

Among these regions, the waist area represents the most critical zone for routing optimization due to the structural interference with the spacesuit waistbelt. During the donning procedure, the Extravehicular (EV) crew member or analog astronaut must tighten the waistbelt firmly. This rigid fixation is mandatory to prevent unwanted shifting, maintain structural balance inside the spacesuit, and stabilize the system's overall center of gravity.

While other structural elements, such as the shoulder straps, also intersect the fluidics layout, their pressure footprint is localized and carries significantly less load compared to the waistbelt.

Figure 13 illustrates the comparative dataset acquired via the localized temperature sensors and complementary infrared thermography. These telemetry assets were deployed during one of the preliminary experimental campaigns aimed at evaluating the baseline performance of the active cooling system.

The left pane of Figure 13 displays a real-time, rotating 3D thermal model that maps the spatial distribution of surface temperatures across the subject's body. For this initial iteration, the sensory architecture comprised six PT1000 RTDs symmetrically paired on the upper limbs, lower limbs, lower back, and anterior torso, respectively. The model's thermal map was realized using a python code then integrated into the simulation software.

At this stage of development, the dedicated Printed Circuit Board (PCB) had not yet been integrated into the system architecture. Consequently, a higher tolerance for signal instability and reduced data integrity was accepted to prioritize the simultaneous assessment of a higher sensor count. Following this troubleshooting phase, the telemetry layout was optimized and streamlined into the definitive configuration detailed previously, which utilizes four PT1000 sensors coupled with a single, multi-parametric Movesense IMU node.

The real-time telemetry visualized on the 3D model highlights a critical fluidic failure mode: the inlet conduit supplying the left lower limb is completely occluded. This obstruction severely restricted coolant propagation, directly caused by a localized pressure point induced by the compressive load of the spacesuit waistbelt.

This phenomenon is corroborated by the right pane of Figure 13, which presents an infrared thermogram of the Extravehicular (EV) wearing the active thermal garment inside the spacesuit. To facilitate direct visual validation via the thermal camera, the outer protective layers of the suit were partially retracted. The resulting thermographic signature explicitly underscores the thermal divergence between the two lower extremities, visually confirming the complete loss of cooling efficiency in the left leg due to mechanical throttling.

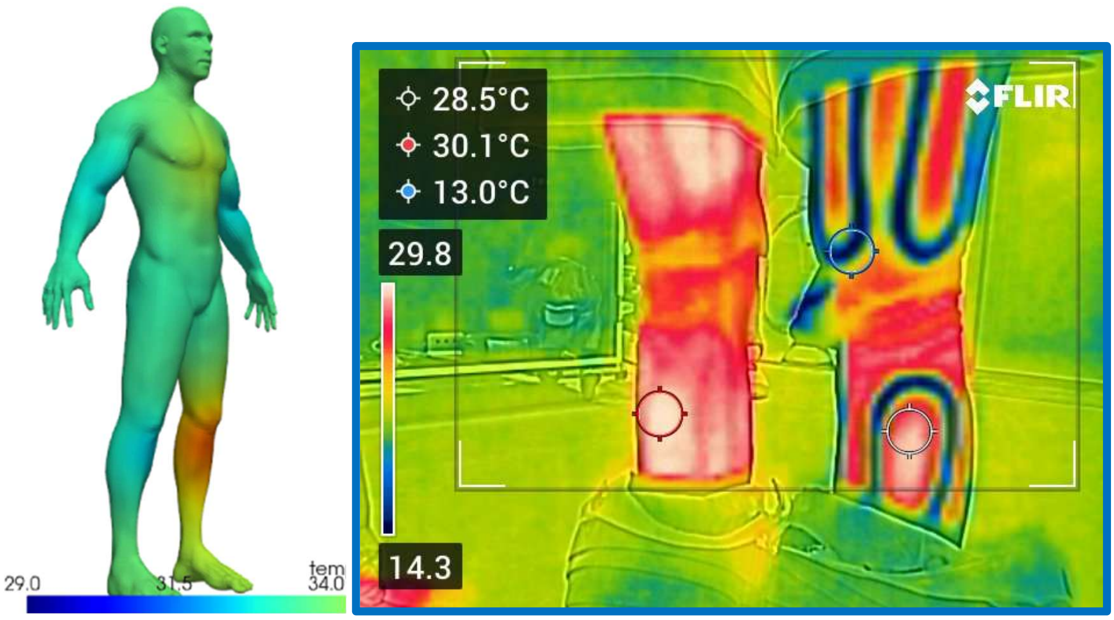

Figure 13 *Temperature sensors data visualization*

Consequently, experimental campaigns demonstrated that isolating and implementing mechanical conduit protections solely within the waist zone was sufficient to entirely mitigate the risk of fluidic occlusion.

Figure 14 displays the temperature profiles recorded by four localized sensors distributed symmetrically across the limbs (two on the upper extremities and two on the lower extremities). Additionally, core body temperature and heart rate were monitored using a chest-mounted Movesense sensor. Utilizing its integrated Inertial Measurement Unit (IMU), this sensor can simultaneously track acceleration and velocity vectors, offering the potential to map and correlate specific EV physical activities with metabolic heat generation.

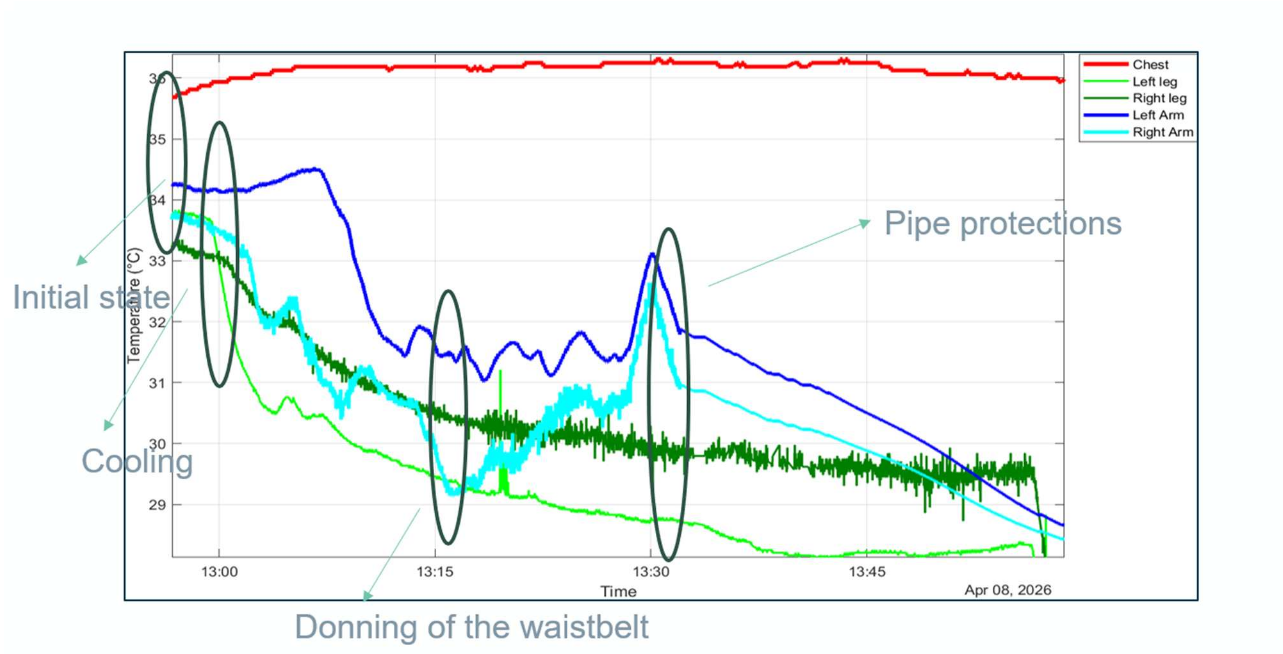

Figure 14 *Waistbelt testing activity*

The initial phase of the experimental timeline reflects the baseline physiological state, during which the sensors recorded nominal skin temperatures prior to activating the active thermal control system. Upon activation, the coolant flow rate was set to its maximum operational threshold of 400 mL/min to evaluate system behaviour under peak fluidic loads.

Following the activation of the active thermal control system, the initial temperature decline recorded across the limbs exhibited a non-linear transient behaviour. This phenomenon was particularly pronounced in the right upper extremity, where thermal stabilization was delayed.

From a fluid dynamics perspective, this latency is attributed to the asymmetric architecture of the fluidic routing: the primary coolant inlet is positioned on the left side of the garment, meaning the fluid path to the right arm is significantly longer. Consequently, the initial flow had to overcome greater cumulative internal friction and hydraulic resistance before the conduits could achieve thermal equilibrium.

The observed temporal delay in the temperature stabilization of the right upper extremity, compared to its left counterpart, can be analytically evaluated through localized fluid dynamics and hydraulic resistance modelling. Prior to achieving a steady-state thermal regime, the transient behavior of the coolant propagation is strictly dictated by the geometric configuration of the internal fluidic routing.

Because the primary coolant inlet is positioned on the left side of the garment, the volumetric path supplying the right arm possesses a significantly greater total length$\left(L_{right} - L_{\text{left}}\right)$. For a fully developed laminar flow within a cylindrical conduit, the internal hydraulic resistance (R_h) is governed by the Hagen-Poiseuille law [29]:

$$R_h = \frac{8\mu L}{\pi r^4}$$

where μ represents the dynamic viscosity of the working fluid (water), L is the localized length of the conduit segment, and r is the inner radius of the pipe.

According to this relation, the hydraulic impedance scales linearly with the length of the channel. Consequently, the longer routing required to reach the right arm introduces a higher cumulative resistance.

Operating under a constant differential pressure (ΔP) supplied by the circulation pump, the volumetric flow rate (Q) is inversely proportional to this resistance ($Q = \Delta P / R_h$).

Therefore, the initial fluid front in the right upper branch requires a longer transient period to overcome the initial viscous shear stress and internal friction. This spatial and structural asymmetry directly accounts for the non-linear cooling curves and the pronounced thermal latency captured by the telemetry sensors before system-wide stabilization is established.

The subsequent tightening of the waistbelt induced distinct thermal fluctuations. Specifically, a localized temperature rebound was observed in the upper extremities. This warming trend directly correlates with the partial occlusion of the inlet conduits supplying the arms, induced by the high compressive stress exerted by the tightened harness.

To mitigate this mechanical throttling, protective U-shaped clips were fabricated via 3D printing using Thermoplastic Polyurethane (TPU) and strategically placed over the conduits along the waistline. These components were engineered to absorb external structural loads and safeguard fluidic patency.

As demonstrated by the subsequent telemetry profiles, the application of these 3D-printed clips immediately successfully resolved the occlusion, allowing the upper extremity temperatures to resume a stable, steady-state decline. Conversely, the temperature profiles of the lower limbs, most notably the right leg, exhibited minor persistent oscillations; these fluctuations were determined to be an artifact of sensor instability and localized thermal coupling rather than structural fluidic issue.

Figure 15 *TPU clips*

As depicted in Figure 15, the structural geometry of these clips was tailored to satisfy two contrasting requirements: providing a wall thickness sufficient to deflect the compressive force exerted by the tight harness, while maintaining a non-rigid profile against the user's skin to prevent pressure points.

TPU was selected as the optimal material for this application due to its unique elastomeric properties, high abrasion resistance, and favourable mechanical compliance. Unlike rigid polymers, TPU exhibits an excellent balance between structural stiffness and flexibility; it yields progressively under high localized pressures, distributing the load evenly over a wider surface area to ensure ergonomic comfort without compromising the cross-sectional integrity of the underlying cooling channels.

From a design and operational perspective, these protective clips feature a compact longitudinal length of approximately two centimetres. Their structural profile is engineered to seamlessly snap directly onto the fluidic conduits, leveraging the inherent elasticity of the TPU material to establish a secure interference fit. This snap-on mechanism eliminates the requirement for additional mechanical locking systems, adhesives, or fasteners, thereby simplifying the integration phase.

Furthermore, this fastener-free architectural approach provides high modular deployment flexibility. The clips can be dynamically repositioned along the fluidics routing based on individual anthropometric measurements or specific suit configurations. While the primary experimental validation focused on mitigating waistline occlusion, the clips can be distributed at the waist zone, the shoulder strap intersections, or concurrently across both high-pressure regions, offering a scalable solution to safeguard system-wide fluidic continuity.

Beyond its utility for post-test data analysis, the real-time 3D thermal mapping interface represents a critical tool for Extravehicular Activity (EVA) operations and biomedical monitoring. By providing an instantaneous, intuitive visualization of surface temperature distribution, ground controllers and medical support teams can directly assess the physiological status, thermal comfort, and localized heat stress of the EV crew member.

Furthermore, this telemetry framework can be leveraged to establish structured operational decision-making matrices and contingency protocols based on localized skin temperature thresholds. For instance, in the event of an active thermal control loop anomaly or conduit occlusion, the system allows mission control to differentiate the severity of the failure based on anatomical location:

- **Critical Core Abort:** A localized occlusion in high-metabolic or core-critical zones, such as the anterior torso (chest) or lower back, would trigger a rapid temperature spike. Because these regions are vital for core thermoregulation, such a failure would dictate an immediate abort of the simulation or EVA operation to prevent heat exhaustion or hyperthermia.
- **Degraded Contingency Operations:** Conversely, if the telemetry indicates a localized occlusion restricted solely to the lower extremities (legs), the core thermal inertia might remain within acceptable safety margins. In this scenario, operations could be safely downgraded or continued under strict monitoring, avoiding an unnecessary mission termination.

Crucially, implementing an objective, sensor-driven monitoring system mitigates risks associated with the human factor. Historical operational data and aerospace medicine literature indicate that crew members frequently misreport or underestimate their physiological discomfort—such as thermal stress or physical fatigue—due to cognitive bias, overestimation of their physical capabilities, or a psychological drive to complete the mission objectives. Furthermore, during high-workload scenarios, individuals may suffer from degraded situational awareness, leaving them genuinely unaware of the onset of heat-related physiological decline.

Because human safety is the absolute priority in any high-fidelity simulation or aerospace operation, relying solely on subjective crew feedback is insufficient. Constant, real-time telemetry monitoring provides an empirical, redundant layer of safety, ensuring that critical medical interventions or abort decisions are based on objective physiological data rather than compromised self-assessments.

In addition to operational monitoring, infrared thermography serves as a critical redundant diagnostic system in the event of primary telemetry degradation or sensor failure. If the embedded PT1000 sensors or the Movesense IMU node experience structural damage, signal drift, or electrical disconnection during a simulation, the real-time data stream becomes compromised. Under these conditions, the thermal camera provides an independent, non-invasive validation method to cross-reference and verify the actual thermal state of the Extravehicular (EV) simulator. When primary sensor telemetry is compromised, open communication channels between the EV and mission control become paramount to bridge the data gap with subjective comfort ratings. To systematically verify the physical integrity of the active cooling loop without disrupting the mission timeline, specific inspection windows can be integrated into the simulation protocol.

During scheduled operational breaks, for instance, every 30 minutes, the spacesuit is temporarily secured on a dedicated structural stand. During these intervals, the outer protective layers of the suit can be partially retracted, allowing support teams to utilize the thermal camera for direct visual inspection. This procedural framework enables the rapid identification of localized structural issues, fluidic chokepoints, or hardware damages that occurred during active simulation phases, ensuring system integrity is maintained throughout the testing campaign.

4.6 CFD Simulations and analytical considerations

To rigorously cross-reference the empirical data gathered by the sensor network and validate the underlying physical phenomena, Computational Fluid Dynamics (CFD) simulations were implemented utilizing ANSYS Fluent.

Because the active thermal control loop relies on Commercial Off-The-Shelf (COTS) components, the primary objective of the numerical campaign was not the geometric dimensioning or structural design of the fluidic system. Instead, the simulations targeted the characterization of the structural and operational limitations of the conduits under mechanical compression. Specifically, the CFD study explores the internal behaviour of the fluid under localized throttling and establishes the deformation thresholds beyond which the heat extraction capacity is no longer considered acceptable or safe for the crew member. The purposes are the following:

1. Characterize fluid behaviour under concentrated mechanical load.

2. Define the structural deformation thresholds of the conduits.

3. Establish the operational boundary for acceptable heat extraction.

Looking toward future system iterations, this computational framework could potentially be integrated directly into the mission control ground segment to act as an inverse predictive model. Instead of relying solely on physical flowmeters, which add weight, complexity, and failure points to the wearable system, the validated CFD curves can be embedded into the ground telemetry consoles to back-calculate unmeasurable internal parameters in real time.

Operationally, this is achieved by continuously monitoring the temperature differential ($\Delta T = T_{\text{out}} - T_{\text{in}}$) across the inlet and outlet manifolds. Under a fixed metabolic heat load, a reduction in the coolant mass flow rate ($\dot{m}$) fundamentally alters the fluid's residence time inside the heat exchanger, causing a non-linear shift in the recorded ΔT.

By mapping the empirical ΔT against the numerical dataset generated via ANSYS Fluent, the ground segment software can perform an instantaneous inverse optimization (Figure 16) . Because a specific volumetric flow rate reduction and a precise percentage of mechanical conduit deformation correspond to a unique thermal signature, the system can simultaneously estimate:

1. **The transient mass flow rate** ($\dot{m}$): Detecting fluidic stagnation or throttling caused by increased hydraulic impedance.
2. **The geometric deformation threshold:** Quantifying the exact physical crush percentage of the tube (e.g., a 40%, 60%, or 80% localized reduction in the cross-sectional area).

Consequently, if a structural deformation takes place under a heavy harness load, the console will not simply flag a generic cooling drop. By coupling the thermal readings with the CFD boundary conditions, it will output a quantitative diagnostic status, estimating both the residual fluid velocity and the physical integrity of the conduit, thereby serving as a virtual sensor for advanced space suit health monitoring.

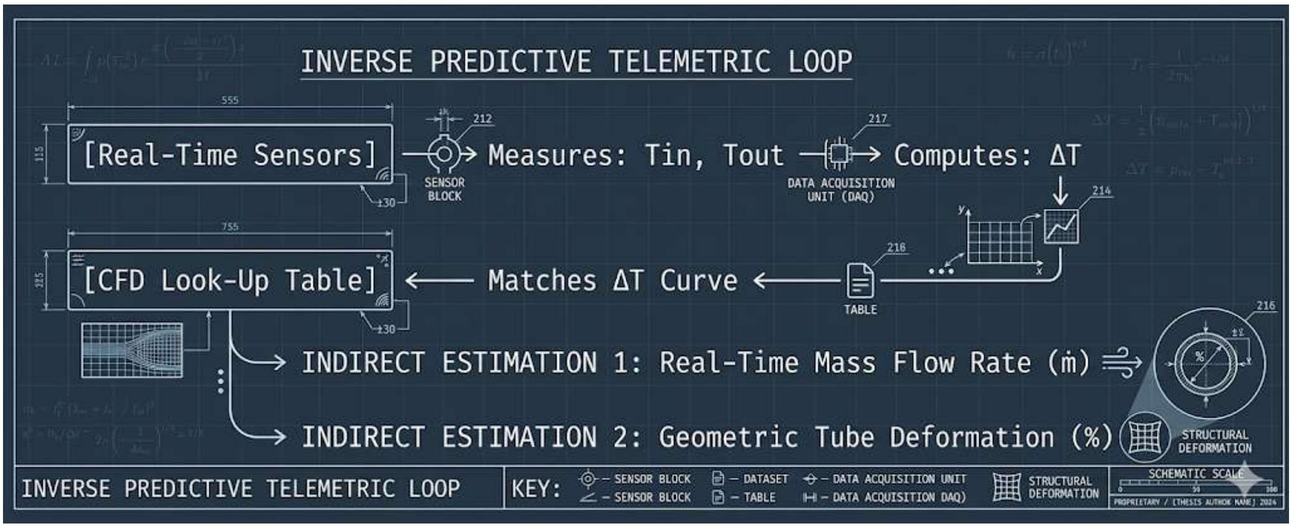

Figure 16 *Inverse predictive telemetric loop*

To ensure computational efficiency and reduce modelling complexity while maintaining high physical fidelity, the numerical study presented herein isolates the anterior torso (chest) conduit routing. This specific region was selected because the chest represents the zone with the highest metabolic heat flux and maximum heat extraction density within the garment layout. Consequently, analysing this branch under varying levels of mechanical deformation provides a conservative, worst-case baseline for the thermal performance of the entire system.

4.6.1 Simulations

The numerical validation workflow was initiated by generating the three-dimensional fluid domain geometry within Autodesk Fusion. The baseline conduit architecture was developed utilizing the "sweep" feature, replicating a circular cross-section with an internal diameter of 6 mm to precisely match the nominal dimensions of the physical Liquid Cooling Garment (LCG) tubing.

To systematically evaluate the fluid dynamics under varying structural conditions, the CAD models were geometrically modified downstream of the inlet boundary condition. Localized mechanical deformations were explicitly modelled by compressing the cross-section into an elliptical profile over a finite longitudinal path. To map the operational boundaries of the cooling loop, four discrete structural scenarios were established and analysed:

- **Nominal Scenario:** unconstricted conduit geometry with zero mechanical deformation (0 mm).
- **Moderate Deformation:** A localized cross-sectional compression of 2 mm along the minor axis.
- **Severe Deformation:** A localized cross-sectional compression of 4 mm along the minor axis.
- **Critical Occlusion:** Near-complete physical throttling of the conduit clearance to evaluate the upper limit of hydraulic impedance.

Following the geometric definition, the fluid domain was imported into ANSYS Fluent, which served as the integrated platform for both the computational meshing and the finite volume fluid dynamic resolution. During the discretization phase, a structured inflation layer was applied along the pipe walls, defining the fluid-structure perimeter as the boundary surface.

This meshing strategy is mathematically mandatory to capture the high velocity and thermal gradients within the hydrodynamic boundary layer. By refining the prismatic cell density adjacent to the wall interface, the simulation ensures an accurate resolution of the viscous shear stress and localized friction coefficients.

Subsequently, advanced conjugate heat transfer (CHT) simulations were conducted to evaluate thermal coupling efficiencies. This secondary campaign utilized a localized, truncated pipe segment positioned in direct mechanical contact with a secondary solid domain engineered to replicate human metabolic heat flux. By implementing a coupled thermal interface between the fluid and solid boundary faces, the model was capable of resolving the concurrent heat conduction through the solid tissue and the convective heat extraction operated by the internal coolant flow.

Nominal scenario

The preliminary numerical simulation was executed under nominal operational conditions. The geometric routing of the conduit, alongside its corresponding static temperature distribution, is illustrated in Figure 17. Within this control scenario, the fluid domain maintains a constant, unconstricted internal diameter of 6 mm across its entire longitudinal path.

To optimize computational efficiency and avoid complex mesh generation for thin solid domains, the physical silicone sheath of the tubing was not explicitly modelled in the CAD geometry. Instead, it was integrated directly within the ANSYS Fluent pre-processor via the boundary conditions setup.

By editing the wall boundary properties, the **Shell Conduction** macro was activated, enabling the virtual discretization of two distinct, layered solid domains directly on the fluid-bounding faces:

1. An innermost layer replicating the **silicone sheath**, configured with a thickness of 1 mm.
2. An outermost layer replicating the **human skin** on the chest, configured with a representative thickness of 1 cm.

The specific thermophysical properties assigned to the fluid (liquid water extracted from the ANSYS database) and the customized solid shells are summarized in Table 6 [30,31,32]:

Material	Water liquid	Silicon	Skin
cp (specific heat) $\left[\frac{J}{kg\ K}\right]$	4186	1200	3500
ρ (density) $\left[\frac{kg}{m^3}\right]$	1000	1100	1050
k (thermal conductivity) $\left[\frac{W}{m\ K}\right]$	0.6	0.2	0.4

Table 6 *Materials thermophysical properties*

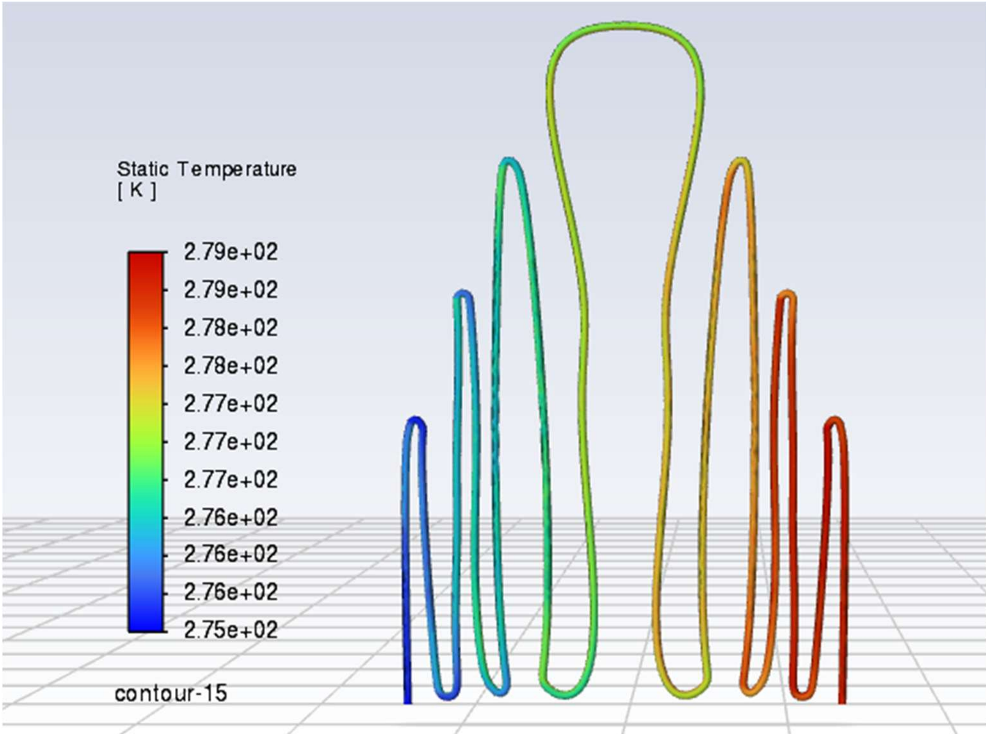

Figure 17 *Temperature distribustion under a nominal scenario*

To resolve the simultaneous fluid flow and conjugate heat transfer, the energy equation was enabled within the solver. Consequently, the computational domain is governed by the steady-state, laminar Navier-Stokes system of equations [29]:

- Continuity equation:

$$\frac{\partial \rho}{\partial t} + \nabla \cdot (\rho \vec{v}) = 0$$

- Momentum equation:

$$\frac{\partial}{\partial t}(\rho \vec{v}) + \nabla \cdot (\rho \vec{v} \vec{v}) = -\nabla p + \nabla \cdot (\bar{\bar{\tau}}\} + \rho \vec{g} + \vec{F}$$

- Energy equation:

$$\frac{\partial}{\partial t}(\rho E) + \nabla \cdot \big(\vec{v}(\rho E + p)\big) = \nabla \cdot \big(k_{eff} \nabla T - \sum_j h_j \vec{J_j} + (\bar{\bar{\tau}}\}_{eff} \cdot \vec{v}\big) + S_h$$

For an incompressible Newtonian fluid like liquid water ($\rho = \text{const.}$), the governing equations simplify as follows:

- **Continuity Equation**

$$\nabla \cdot v = 0$$

- **Momentum Equation**

$$\rho(v \cdot \nabla)v = -\nabla P + \mu \nabla^2 v$$

- **Energy Equation**

$$\rho c_p (v \cdot \nabla T) = k \nabla^2 T$$

When enabled the **Laminar** model alongside the **Energy Equation** in Ansys Fluent, the solver couples the fundamental laminar Navier-Stokes equations with the first law of thermodynamics to resolve fluid flow and heat transfer without any turbulent transport terms. Specifically, Fluent solves the **Continuity Equation** for mass conservation if incompressible ($\frac{\partial \rho}{\partial t} + \nabla \cdot (\rho \vec{v}) = 0$) and the **Laminar Momentum Equation**, where the stress tensor (τ) depends solely on the fluid's molecular dynamic viscosity (μ) rather than turbulent Reynolds stresses. Concurrently, the **Energy Equation** governs thermal transport, simplifying the heat diffusion term to utilize only the material's molecular thermal conductivity (k). Other phenomena within the energy balance, such as species diffusion ($\sum_j h_j \vec{J_j}$) or volumetric heat sources (S_h), are only computed if specific models like species transport or radiation are activated, while the viscous dissipation term (viscous heating) remains disabled by default unless manually checked for highly viscous or high-velocity flows.

The values corresponding to the nominal case are gathered in Table 7.
The boundary conditions implemented to resolve the nominal control case were derived directly from experimental data and component specifications:

- **Inlet Mass Flow Rate ($\dot{m}$)**: Set to 400 mL/min (equivalent to $6.65 \times 10^{-3} kg/s$), corresponding to the maximum operational output of the miniature circulation pump.
- **Inlet Temperature (T_{in}):** Configured at 275.15 K. This value represents the stabilized temperature of the fluid bladder, monitored experimentally via an integrated light-sensitive thermochromic patch.
- **External Wall Temperature (Skin Baseline):** Constrained at a constant core skin temperature of 310 K.

The localized thermal exchange induces a highly visible temperature gradient within the moving fluid domain, whereas the thermal footprint on the external skin domain exhibits a higher inertia. The fluid temperature shifts from an inlet baseline of 275.15 K to a simulated outlet temperature (T_{out}) of 278.3 K, yielding a net temperature differential (ΔT) of 3.15 K.

Parameter	Value
$\Delta T = (T_{out} - T_{in})$	3.15 °C
$\dot{Q}$ (cooling power)	92.3 W
P (relative inlet pressure)	2800 Pa

Table 7 *Nominal scenario's output*

The Cooling power $\dot{Q}$, representing the system's capacity to extract metabolic heat from the chest area, is computed using the standard calorimetric relation:

$$\dot{Q} = \dot{m} \cdot \mathrm{cp} \cdot \Delta T$$

Where ΔT is the difference in temperature between the inlet and the outlet, and $\dot{m}$ the mass flow rate set in the boundary conditions.

Beyond establishing the baseline heat transfer rate, the primary utility of the nominal simulation is to extract the exact hydraulic boundary conditions required to feed the subsequent deformed scenarios.

In the physical active garment, the overall mass flow rate delivered by the pump remains globally constant. However, the garment's fluidic architecture consists of multiple cooling branches arranged in a **parallel network**.

When a localized mechanical deformation occurs along a specific branch (such as the chest conduit), the localized hydraulic resistance (R_h) of that single pipe spikes exponentially. According to the lumped-parameter fluid network theory, because the constricted branch is in parallel with other unconstricted conduits (e.g., those routing to the limbs), the fluid blocked by the deformation is naturally redistributed into the paths of least resistance.

Consequently, while the mass flow rate ($\dot{m}$) through the deformed chest pipe drops significantly, the relative inlet pressure (ΔP) driving the fluid into that specific branch remains constant and anchored to the system's global operating pressure.

To capture this physical behaviour in the numerical models, the nominal simulation was used to calculate the baseline operating pressure. By integrating the pressure across the inlet cross-section after convergence, a static inlet relative pressure of **2800 Pa** was obtained.

For all subsequent simulation cases involving conduit deformations, the boundary condition at the inlet was switched from a fixed *Mass Flow Inlet* to a fixed *Pressure Inlet* constrained at 2800 Pa. This methodological framework ensures an accurate, high-fidelity replication of the parallel network behaviour, directly evaluating how the mass flow rate, and consequently the cooling power, declines as a function of a localized deformation length.

This functional degradation directly follows the physical laws governing hydraulic resistance. The fluid dynamic resistance of a conduit branch increases exponentially as its cross-sectional area decreases. When the circular geometry is mechanically compressed into an elliptical profile under the localized footprint of the waistbelt, the total resistance of the constricted zone scales linearly with the length of the deformation and inversely with the geometry of the axes:

$$R_{\text{tot}} = \frac{8\mu(L - L_{\text{deformation}})}{\pi r_{\text{nominal}}^4} + \frac{8\mu L_{\text{deformation}}}{\pi r_{\text{constricted}}^4}$$

Since $\dot{m} = \frac{\Delta P}{R_h}$, $and\ P_{\text{cooling}} = \dot{m} \cdot c_p \cdot (T_{\text{out}} - T_{\text{in}})$, as the hydraulic resistance escalates, both the mass flow rate and the resulting cooling power decrease proportionally. For the subsequent numerical simulations $L_{\text{deformation}}$ was standardized at a fixed length of 2 cm to simplify the geometric meshing process while maintaining high physical fidelity.

Acceptable scenario – 2mm deformation

The second numerical simulation was executed to evaluate system performance under a moderate mechanical constriction, specifically a localized deformation of 2 mm along the axis of the conduit cross-section. Figure 18 illustrates both the global static temperature distribution and a detailed close-up view of the constricted region.

Visually, a 2 mm restriction introduces a subtle geometric variation that does not severely alter the flow path layout. Thermally, the resulting temperature field remains highly comparable to the nominal baseline. Driven by a constant inlet temperature (T_{in} =275.15 K) the fluid exits the domain at T_{out} = 278.6 K, yielding a net temperature differential $(\Delta T)\ of\ 3.45\ K$ This represents an increase of only 0.30 K in the outlet thermal profile compared to the unconstrained scenario.

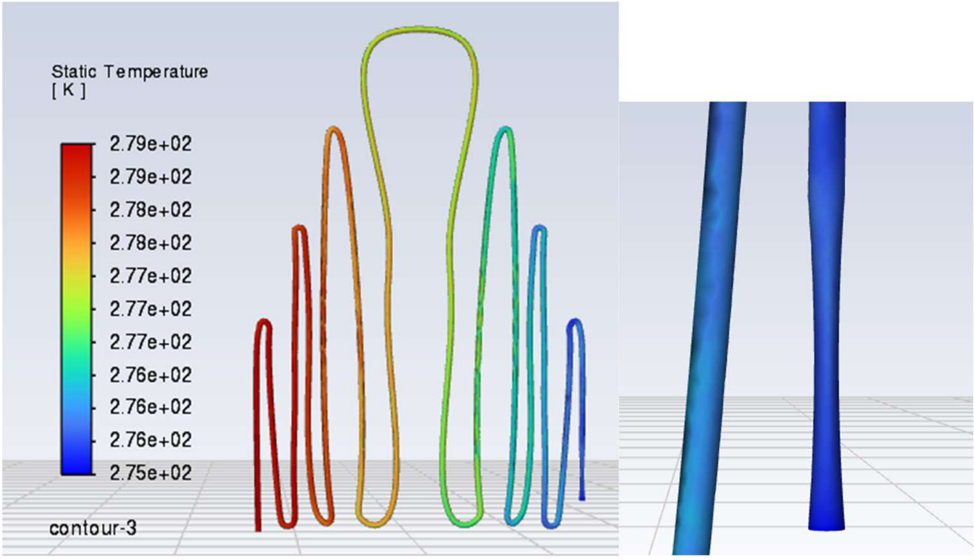

Figure 18 *Moderate deformation: temperature distribution*

This localized temperature increase is physically intuitive: under a constant metabolic heat flux, a reduction in the coolant mass flow rate decreases the total thermal capacity of the moving fluid mass within the branch, making it more susceptible to temperature rises per unit time. However, within the calorimetric cooling power equation, the mass flow rate exerts a dominant linear scaling effect compared to the minor increase in ΔT. The key operational and thermodynamic parameters extracted from this simulation are consolidated in Table 8.

Parameter	Value
Delta T	3.45 °C
Mass flow rate	0.006 kg/s =350 ml/min
$\dot{Q}$ (cooling power)	87 W

Table 8 *Moderate deformation's output*

As evidenced by the numerical dataset, the overall cooling capacity experiences a minor degradation because both the mass flow rate and the temperature differential diverge only slightly from the nominal control baselines:

$$\eta_{2m} = (Q_{2m} / Q_{nom}) * Q_{nom} = 95\% \, \eta_{nom}$$

An interesting physical phenomenon observed in this simulation is that while the global heat removal efficiency drops by 5%, the localized mechanical constriction locally intensifies the heat transfer coefficient (h), as visualized in the heat flux maps of Figure 19. This localized behaviour is governed by Fourier's Law of heat conduction [30]:

$$q = -\lambda \frac{\partial T}{\partial n}$$

where q is the thermal flux, λ is the fluid's molecular thermal conductivity and $\frac{\partial T}{\partial n}$ is the temperature gradient normal to the wall.

Concurrently, the convective heat transfer coefficient (h) is analytically tied to the dimensionless Nusselt number and is inversely proportional to the characteristic hydraulic diameter of the deformed cross-section:

$$h = \frac{Nu \cdot \lambda}{D}$$

When a pipe constricts, fluid velocity increases, which directly enhances the *conductive* heat transfer within the fluid by compressed boundaries. According to the no-slip condition, fluid molecules in direct contact with the pipe wall are completely stationary, forming a microscopic stagnant layer known as the thermal boundary layer (δ_t). Because this thin film of fluid is stationary, heat can only cross it via pure conduction, governed by Fourier's Law. As the narrower pipe forces the fluid to accelerate, the high-velocity flow mechanically shears and thins this boundary layer. With δ_t drastically reduced, the thermal resistance drops, and the temperature gradient $\Delta T/\delta_t$ steepens sharply. Consequently, conduction through this initial fluid barrier becomes significantly faster and more efficient, which is macroscopically observed as a major boost in the convective heat transfer coefficient.

In operational aerospace engineering simulations, if a structural constriction does not severely compromise the global mass flow rate of the parallel network, such localized thermal enhancements can be intentionally leveraged. This phenomenon could potentially be beneficial for redirecting higher heat extraction densities toward critical high-metabolic anatomical zones that require preferential cooling compared to peripheral areas.

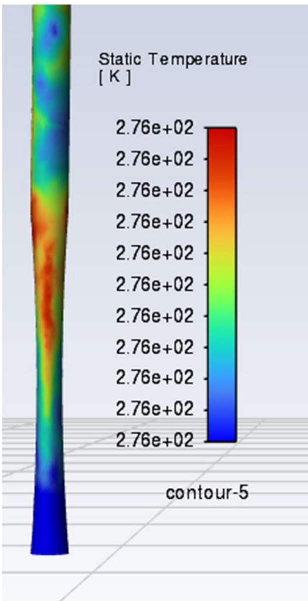

Figure 19 *Temperature in the constriction*

Limit scenario-4 mm deformation

The numerical simulation for the 4 mm deformation scenario establishes the operational boundary for the active thermal loop, representing the maximum allowable structural degradation before the system breaches safety margins. Within the framework of this study, the acceptable performance threshold is defined by a retention of at least 85% of the nominal cooling power baseline. Any structural occlusion inducing a thermal extraction efficiency below this 85% limit classifies the active cooling garment as unreliable and unsafe for sustained Extravehicular Activity (EVA) simulation workloads.

Parameter	**Value**
Delta T	3.65°C
Mass flow rate	0.0051 kg/s
$\dot{Q}$ (cooling power)	78 W

Table 9 *Severe deformation's output*

Within this limit-state scenario, the fluid exit temperature reaches 278.8 K representing an increase of only a few tenths of a Kelvin compared to the nominal control baseline. Across the moderate deformation regimes (2 mm and 4 mm), the absolute outlet temperature profiles exhibit a high degree of similarity. This behaviour demonstrates that a highly localized constriction restricted to a longitudinal footprint of just a few centimetres does not immediately collapse the volumetric transport capacity of the circuit, as the concentrated minor pressure losses and localized friction coefficients have not yet reached the critical threshold required to choke the overall thermal exchange.

From a geometric perspective, the compressed conduit cross-section transitions into an elliptical profile. As long as the minor axis maintains a sufficient clearance to prevent the extreme thickening or stagnation of the hydrodynamic boundary layer, the localized obstruction can still accommodate a functional fluid flow and sustain convective heat transfer.

However, as consolidated in the dataset, the global cooling power experiences a net reduction of 15% relative to the nominal control baseline. The boundary layer thinning phenomenon described in the previous section is further intensified within the 4 mm constriction zone. Due to the higher localized fluid acceleration mandated by the continuity equation, the local convective heat transfer coefficient spikes, causing the localized thermal extraction rate within the restriction to be significantly stronger than in the unconstricted segments of the conduit.

Nevertheless, because the sharp increase in global hydraulic impedance reduces the total mass flow rate distributed to this parallel branch, the system's global heat removal efficiency undergoes a macroscopically quantifiable degradation, even though the localized fluid temperature rises by only a fraction of a degree.

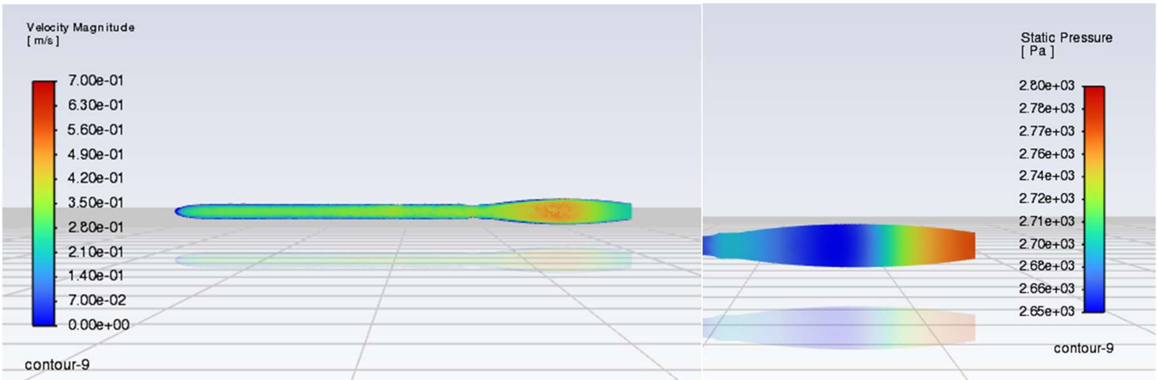

Figure 20 *Velocity magnitude and static pressure in the constriction*

Figure 20 illustrates the internal fluid dynamics extracted from a longitudinal cross-sectional plane of the conduit, mapping the localized variations in velocity and static pressure fields across the constriction zone. In accordance with Bernoulli's principle and the continuity equation for incompressible flows, the reduction in the cross-sectional area forces the fluid to accelerate locally. Concurrently, this localized velocity spike induces a sharp drop in static pressure within the throat of the obstruction. As the fluid exits the deformed segment, it experiences a net permanent pressure drop of approximately 300 Pa compared to the upstream baseline, driven by localized friction and minor viscous dissipation losses.

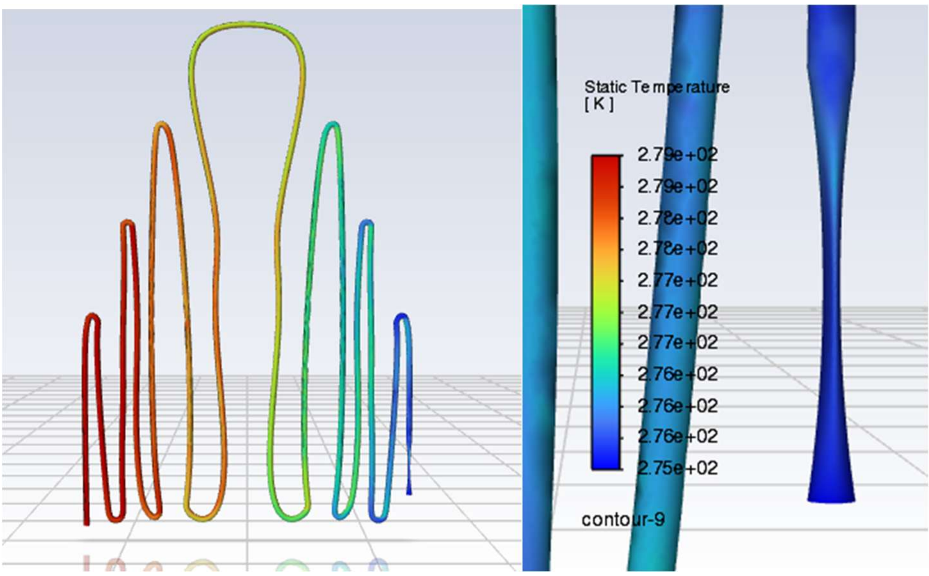

Figure 21 *Severe deformation: temperature distribution*

Furthermore, Figure 21 presents the static temperature contours alongside a detailed close-up view of the 4 mm restriction, where the geometric distortion of the elliptical profile is visibly more pronounced than in the moderate 2 mm scenario. This specific configuration marks the critical limit-state boundary for the active thermal control loop. Beyond this structural threshold, the compounded effects of the elevated hydraulic impedance and the consequent reduction in mass flow rate cause the coupled fluidic and thermal performance of the garment to deteriorate below acceptable safety and operational standards.

Total obstruction

The final simulation investigates a near-complete mechanical collapse of the fluidic channel, where the minor axis of the elliptical profile is restricted to a clearance of just 0.5 mm. This scenario represents an extreme, worst-case occlusion regime that diverges fundamentally from the behaviour observed in the previous three cases.

At this magnitude of compression, the fluid mechanics are no longer governed merely by minor localized flow acceleration. Instead, the concentrated friction coefficients, structural throttling, and the merging of opposing hydrodynamic boundary layers introduce an insurmountable hydraulic resistance. Under the fixed system driving pressure condition, this extreme impedance spike severely chokes the fluid transport, triggering an almost total stagnation of the mass flow rate within the branch. The resulting key thermodynamic and fluidic data are compiled in Table 10.

Parameter	Value
Delta T	8 °C
Mass flow rate	0.0008 kg/s
$\dot{Q}$ (cooling power)	26.8 W

Table 10 *Near-total occlusion's output*

As quantified by the numerical resolution, the global cooling power and thermal extraction efficiency experience a catastrophic collapse, dropping to just 29% of the nominal control baseline. This extreme structural degradation chokes the fluidic path, allowing only a nominal, residual mass flow rate—in the order of a few millilitres per minute—to pass through the obstruction.

Figure 22 displays the static temperature field alongside a detailed visualization of the constriction zone, which is mechanically compressed to such an extent that the fluidic clearance nearly vanishes.

Under these conditions, because the coolant mass flow rate approaches near-stagnation, the fluid residing within the truncated channel reaches thermal equilibrium with the surrounding solid domain almost instantaneously. However, due to the severe deficit in moving fluid mass capable of transporting energy downstream, the net heat capacity rate of the branch drops to a fraction of its operational requirement. This verifies that a 0.5 mm clearance triggers a total failure of the active thermal control mechanism, leaving the corresponding anatomical zone entirely uncooled.

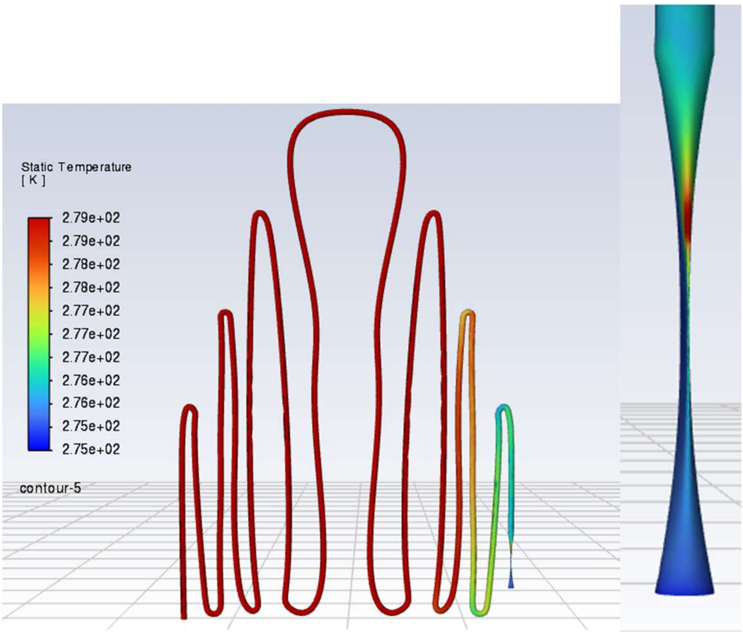

Figure 22 *Near-Total occlusion: temperature distribution*

The coupled fluidic and thermal responses across all evaluated structural configurations are synthesized in the comprehensive chart presented in Figure 23. This diagram maps the direct dependencies of the coolant mass flow rate, the net temperature differential, and the resulting calorimetric cooling power as a function of the localized conduit deformation level.

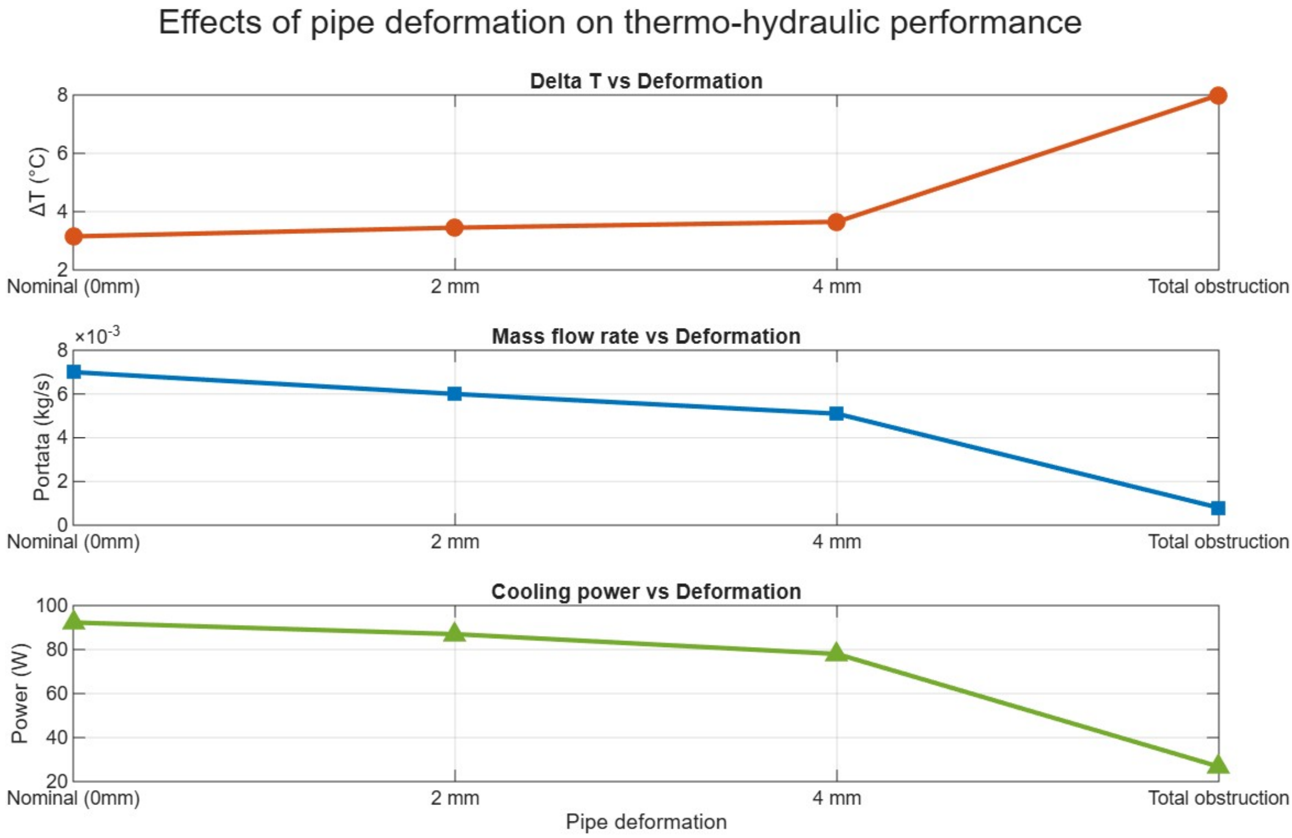

Figure 23 *Effect of pipe deformation on thermohydraulic performance*

The numerical curves reveal a non-linear degradation profile that validates the underlying hydraulic network theory. As long as the mechanical restriction preserves a sufficient cross-sectional clearance to accommodate the required volumetric throughput, the localized fluid acceleration thins the thermal boundary layer, steepening the temperature gradient and maintaining a satisfactory convective heat transfer rate.

However, upon transitioning into the near-total occlusion regime, the astronomical spike in localized hydraulic resistance chokes the flow path. At this juncture, the drastic deficit in moving coolant mass renders the system incapable of transporting energy downstream, resulting in a catastrophic collapse of the global heat extraction capacity.

Consequently, while a localized structural deformation of up to 2 mm falls within acceptable operational safety margins (retaining approximately 95% of the baseline cooling capacity), mechanical degradations exceeding this threshold rapidly converge toward the critical 85% limit-state boundary.

Because these geometric occlusions are induced by external physical loads—such as the tight anchoring of the spacesuit harness or life-support system backplate—and cannot be actively compensated for by the software or the constant-pressure pump architecture, they represent a severe single-point failure risk for the astronaut's thermoregulation.

To mitigate this operational hazard, the implementation of ruggedized physical countermeasures is strictly mandatory. Integrating lightweight, high-stiffness Thermoplastic Polyurethane (TPU) protective clips around vulnerable conduit routings provides the necessary structural reinforcement. These mechanical shells shield the flexible silicone tubing from concentrated external compression, guaranteeing unconstrained fluidic paths and ensuring the long-term reliability of the extravehicular thermal control garment.

The structural scenarios analysed in this study isolate the fluid dynamic and thermal consequences of a single localized deformation. In an operational Liquid Cooling Garment (LCG), while these compressions can occur under the concentrated loads of the waistbelt, empirical testing identifies a more prevalent failure mode at the inlet manifold interface. Specifically, structural throttling frequently occurs at the junction coupling the flexible garment conduits to the fluid bladder ports, where localized bending moments and structural misalignments induce geometric kinking.

To eliminate this vulnerability in future design iterations, the architecture will integrate specialized rigid extensions and strain-relief connectors. These components are engineered to guide the fluid lines along a controlled minimum bend radius, mechanically preventing acute bending at the interface.

In the interim, the deployment of external TPU protective clips fulfils a critical dual-purpose role: they provide radial resistance against compressive loads and act as structural splints. By maintaining the axial alignment of the flexible conduits along high-stress paths, these countermeasures prevent localized occlusions, ensuring a stable mass flow rate and preserving the nominal thermal regulation of the spacesuit system.

Figures 24 and 25 illustrate the transient thermal interaction between the coolant and the human body, modelled as a secondary solid domain with the thermophysical properties of skin tissue. The first case represents the deformed pipe, while the last one shows the nominal scenario.

This analysis maps the localized temperature drop across a truncated conduit segment to evaluate the cooling efficacy exerted on the skin over a localized temporal scale.

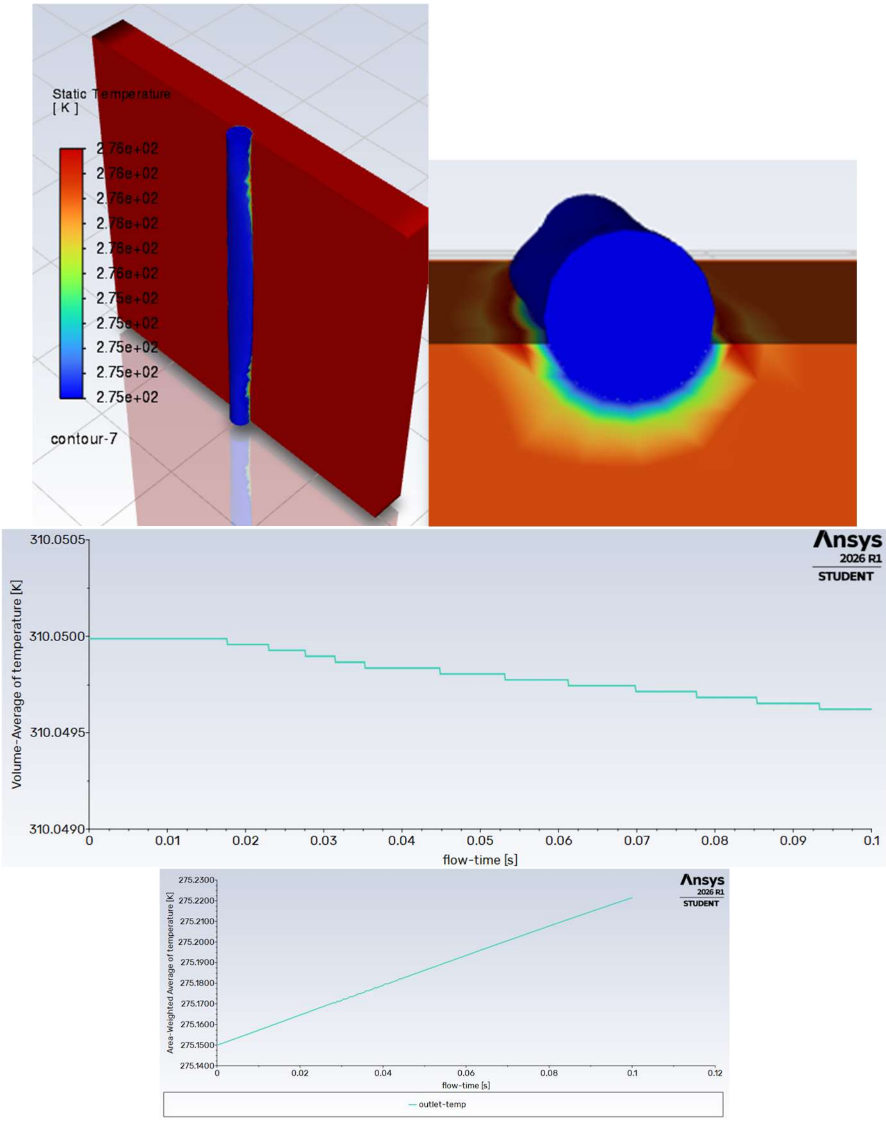

Figure 24 *Interaction between the body and a deformed pipe segment*

Due to computational license constraints and limits on the maximum allowable mesh element count, a full-length pipe simulation with the coupled solid domain was not feasible; hence, a truncated segment was utilized.

Despite this geometric restriction, the numerical results successfully capture the immediate conjugate heat transfer dynamics occurring during the brief fluid residence time.

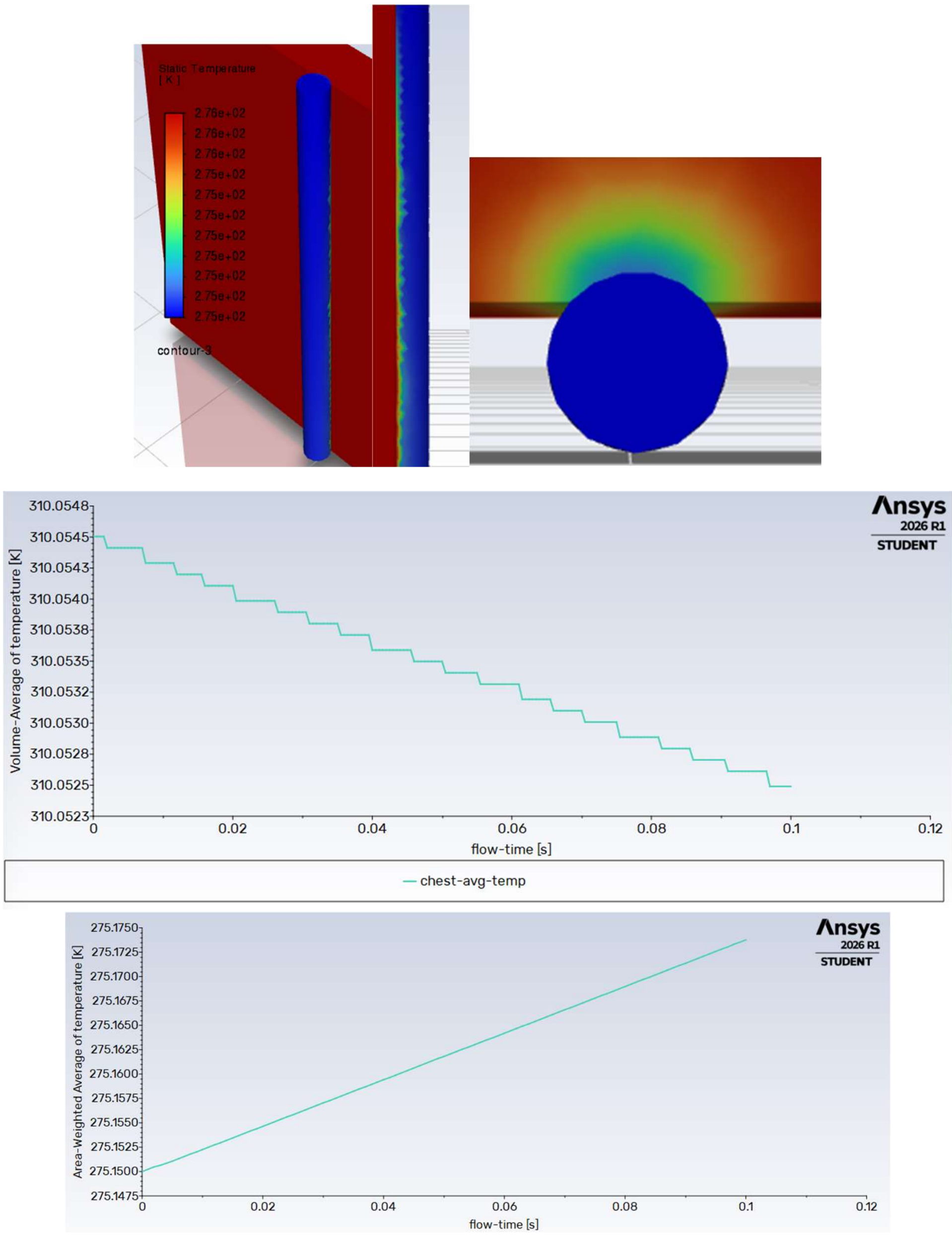

Figure 25 *Interaction between the body and a nominal pipe segment*

Despite implementing a highly narrow temperature scale to resolve fine thermal variations, a stark divergence between the two configurations is readily observable. The compressed conduit exhibits accelerated fluid warming within the constricted zone, which reduces its downstream cooling capacity.

To achieve these coupled results, a multi-domain thermal coupling was implemented, requiring the explicit definition of fluid-solid and solid-solid boundary interfaces. This modelling choice significantly increased the topological complexity of the mesh, demanding a highly refined grid resolution at the interlocking face boundaries to ensure energy conservation across the domains.

Consequently, due to these high computational overheads and hardware element-count constraints, full-scale garment simulations were not feasible within this study. However, utilizing a high-performance computing (HPC) cluster would allow the entire multi-branch cooling network to be modelled directly atop a high-fidelity anthropomorphic human body mannequin. Such an advanced computational framework would yield highly precise, time-dependent spatial distribution data regarding metabolic heat extraction and localized skin temperatures.

4.7 Hardware modification

To accommodate the newly developed active cooling loops within the suit architecture, several mechanical and structural upgrades were implemented, as illustrated in Figure 26. First, a redesigned Portable Life Support System (PLSS) enclosure was developed and fabricated via additive manufacturing (3D printing). The primary design objective was to introduce an openable, modular configuration to facilitate rapid replacement of the cooling bladders and optimize the internal routing and management of the fluidic and electronic subsystems.

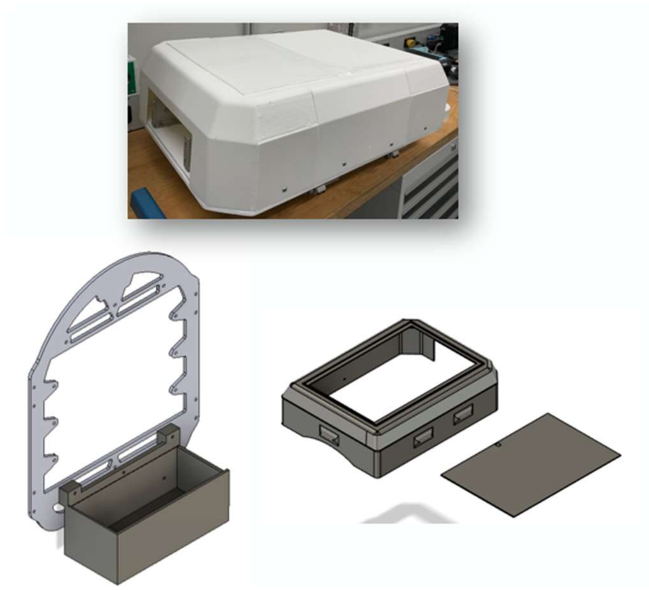

Figure 26 *Suit hardware modifications*

Due to the volumetric envelope constraints of the 3D printer bed, the primary PLSS chassis was sectioned into six distinct components. These modules were subsequently integrated using a high-fidelity fastening layout consisting of nuts and bolts recessed into dedicated, form-fitting housings. Each joint interface featured an integrated hexagonal slot engineered to capture and retain the nut against rotational forces on one side, paired with a counter-bored clearance opening and a load distribution shoulder on the opposite side to seat the fastening bolt securely.

Once fully assembled, the segmented enclosure was secured to the primary structural metal plate of the PLSS backplate utilizing eight structural screws—four symmetrically distributed on each side. The superior section of the chassis integrated linear guide rails designed to accommodate a translationally sliding access lid. Two distinct manufacturing methodologies were evaluated for the fabrication of this sliding interface:

1. A segmented, four-piece additive manufacturing layout assembled post-printing.
2. A monolithic polymethyl methacrylate (PMMA / Plexiglass) variant produced via laser cutting and subsequently wrapped in a white protective vinyl film.

To decouple the fluid storage from the primary structural shell and eliminate the need to place the entire cooling backpack assembly directly inside the PLSS, a dedicated bladder retention bracket was designed. This bracket allowed the fluid bladder to be anchored directly to the rigid PLSS backplate, enabling swift access and replacement through the upper sliding lid aperture without requiring a full system disassembly.

Furthermore, a custom enclosure was designed for the Raspberry Pi micro-controller unit. This housing featured a sliding lid mechanism and integrated slot cutouts to facilitate the routed passage of the instrumentation and temperature sensor cables, significantly streamlining the packaging of the electronic bus.

During the operational donning procedure, the array of temperature sensors was secured beneath the liquid cooling garment utilizing biometric adhesive tape. The integrated Raspberry Pi enclosure was then integrated into the PLSS, as demonstrated in Figure 27.

The sensor wiring harnesses remain exposed in the visualization, routing directly into the micro-controller housing housed within the PLSS cavity via a hook-and-loop (Velcro) mounting interface. Throughout the suit donning sequence, the electronics enclosure was guided through the dedicated left-lateral bulkhead aperture of the suit torso, positioned adjacent to the helmet ring interface.

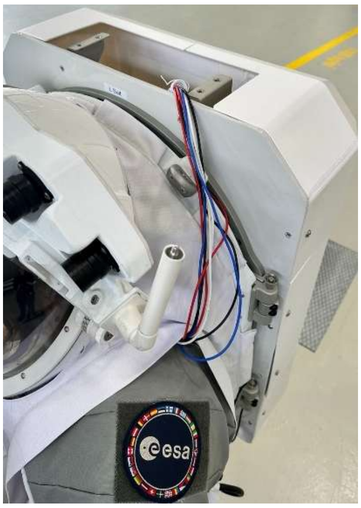

Figure 27 *Wires connecting the sensors to Raspberry Pi stored in the PLSS*

5 Bio-Thermal Modeling and Predictive Control Architecture

5.1 Next-Step Hardware Integration

To transition toward an automated, autonomous, or AI-driven thermal regulation system within the LUNA facility, defining an objective driver parameter is essential for establishing real-time control loop requirements. While localized skin temperature is a direct physiological indicator, it remains highly subjective; baseline body temperatures, metabolic conditioning, and individual comfort thresholds vary significantly among human subjects. Furthermore, skin temperature exhibits a substantial thermal lag, reacting only after metabolic heat has already accumulated in the tissue.

A more robust and predictive control driver is the metabolic rate, or Rate of Energy Expenditure (REE), which quantifies the instantaneous thermal power generated by the human body during varying physical workloads. To decouple the control system from individual subjectivity and sensor latency, an indirect metabolic assessment must be implemented via the mathematical framework of indirect calorimetry [33].

As an immediate development and operational next step for physical integration into the LUNA spacesuit mock-up, the monitoring and control signals must be hardwired to the physical switches located on the suit's front panel (replicating the Display and Control Module - DCM used in standard NASA Extravehicular Activities). This integration allows the astronaut to override the autonomous system and manually control the cooling levels via the front switches. To implement this hardware loop, the immediate technical objective is to analyse the raw signal profiles using a digital oscilloscope.

By probing the electronic interfaces of the front panel toggle switches, the oscilloscope will map the voltage transients, signal frequencies, and duty cycles generated upon manual actuation. Once these electrical signatures are characterized, a micro-controller or Data Acquisition (DAQ) interface can bridge the physical toggle actions to the software control loops, allowing the system to seamlessly switch between the fully autonomous predictive mode and manual astronaut-driven cooling overrides.

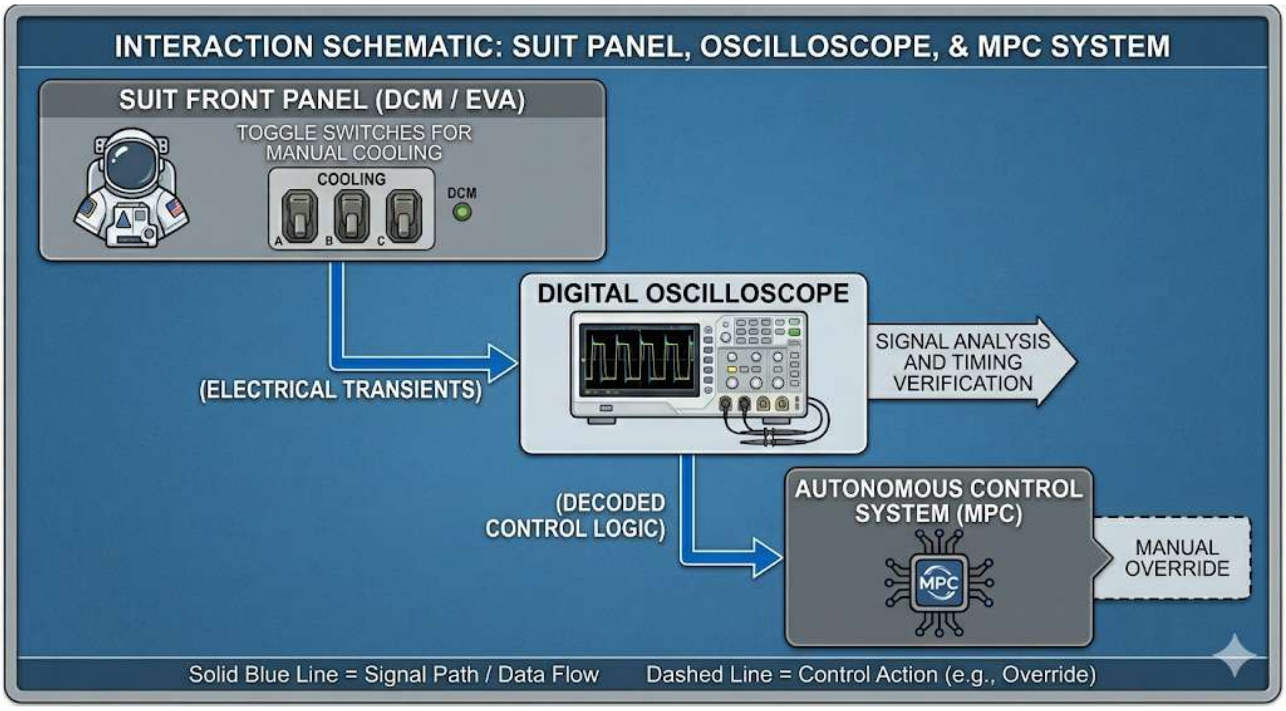

Figure 28 *Evolution from Suit Panel to MPC system*

5.2 Indirect Calorimetry and the Expanded Weir Framework

Indirect calorimetry relies on fundamental biochemical principles, where the metabolic oxidation of energy substrates (carbohydrates, lipids, and proteins) consumes oxygen (O_2) and produces carbon dioxide (CO_2) in known stoichiometric ratios [33]. By monitoring respiratory gas exchange via flow sensors and gas analysers integrated within the Life Support System helmet loop, the instantaneous metabolic heat generation can be calculated in real time.

The comprehensive relation developed by J. B. de V. Weir (1949) eliminates the operational necessity of tracking urinary nitrogen excretion for short-term automated applications, introducing an elegant simplification that aggregates the thermodynamic energy equivalent of macronutrient combustion. Under standard physiological conditions, the metabolic oxidation of 1 Liter of pure oxygen yields approximately 4.68 kcal when burning lipids, and up to 5.05 kcal when burning pure carbohydrates.

Weir's mathematical framework accounts for this fluctuating substrate mixture by pairing the oxygen uptake with the corresponding carbon dioxide production, capturing the instantaneous Respiratory Quotient ($RQ = \dot{V}\mathrm{CO_2}/\dot{V}\mathrm{O_2}$). The classic non-protein Weir equation determines the instantaneous metabolic energy expenditure ($M_{\mathrm{Weir\_kcal}}$) as follows [34,35]:

$$M_{\mathrm{Weir\_kcal}} = 3.9 \cdot \dot{V}\mathrm{O_2} + 1.1 \cdot \dot{V}\mathrm{CO_2}$$

where $\dot{V}\mathrm{O_2}$ represents the volumetric oxygen consumption rate [L/min] and $\dot{V}\mathrm{CO_2}$ is the carbon dioxide production rate [L/min].

The fixed coefficients 3.9 and 1.1 are mathematically derived from the precise caloric values of respiratory gases: the constant 3.9 reflects the baseline energy released per liter of consumed oxygen, while the addition of $1.1 \cdot \dot{V}CO_2$ acts as an automatic correction factor for the metabolic shifting between fats and carbohydrates. This formulation provides a highly accurate energy estimate (with an inherent error margin of less than 1%) regardless of the subject's exact nutritional state or shifting diet.

The resulting energy expenditure is yielded in kcal/min. To integrate this metabolic input into the active garment's control loop, the value is converted into the International System unit of power (Watts) utilizing the standard thermodynamic conversion factor (1 kcal/min = 69.733 W):

$$M_{\text{Weir}}(t) = M_{\text{Weir\_kcal}}(t) \cdot 69.733$$

Since the human respiratory tract expels the totality of metabolically produced carbon dioxide directly into the helmet cavity, the integrated gas sensors intercept the metabolic gas exchange at the source, ensuring that $M_{\text{Weir}}(t)$ provides an absolute, real-time measurement of the total energy generated by the subject.

5.3 Thermodynamic Apportionment of Metabolic Energy

From a thermodynamic perspective, the gross metabolic power (M_{Weir}) does not entirely degrade into a heat load that burdens the liquid cooling system. In accordance with NASA bioengineering standards for extravehicular activity (EVA) life support design, the total metabolic energy must be partitioned into specific thermodynamic sinks: mechanical work, respiratory/evaporative heat losses, and net conductive heat transfer to the Liquid Cooling Garment (LCG) [42].

The macro-level energy balance of the human body enclosed within the suit system is governed by the conservation of energy:

$$M_{\text{Weir}}(t) = W_{\text{mechanical}}(t) + Q_{\text{respiration}}(t) + Q_{\text{perspiration}}(t) + Q_{\text{cooling}}(t)$$

5.3.1 Mechanical Efficiency Offset (10%)

During physical locomotion, a portion of the metabolic energy is converted into external mechanical work ($W_{\text{mechanical}}$) to move the limbs and overcome the structural resistance of the pressurized suit layers. This conversion is dictated by the human mechanical efficiency (η), defined as:

$$\eta = \frac{W_{\text{mechanical}}}{M_{\text{Weir}}}$$

In alignment with standard NASA physiological models for moderate ambulation, the human mechanical efficiency is evaluated at $\eta = 0.10$ [36,42]. Therefore, 10% of the gross metabolic power is mechanical work dissipated into the environment, leaving 90% of M_{Weir} as internal heat generation (Q_{internal}):

$$Q_{\text{internal}}(t) = (1 - \eta) \cdot M_{\text{Weir}}(t) = 0.90 \cdot M_{\text{Weir}}(t)$$

5.3.2 Respiratory and Basal Evaporative Dissipation (14%)

The human body naturally expels heat through the respiratory tract and baseline skin transpiration without requiring active liquid refrigeration. According to NASA life support benchmarks, this baseline non-hydraulic dissipation accounts for approximately 14% of the total metabolic expenditure ($Q_{\text{respiration}} + Q_{\text{perspiration}} \approx 0.14 \cdot M_{\text{Weir}}$) [42,43].

This 14% fraction is split into specific physical mechanisms:

1. Respiratory Sensible Heat Loss ($Q_{\text{res,s}}$): The thermal energy required to raise the temperature of the inhaled dry air from the helmet inlet temperature (T_{inlet}) to the core body temperature (≈ 37°C).
2. Respiratory Latent Heat Loss $\left(Q_{\text{res,l}}\right)$: The energy consumed by the phase change of liquid water evaporating inside the lungs to fully saturate the exhaled breath.
3. Basal Perspiratio Insensibilis ($Q_{\text{per,basal}}$): The continuous, passive diffusion of water vapor through the skin layer occurring independently of active sweating.

5.3.3 Net Hydraulic Cooling Target (76%)

Subtracting the 10% mechanical work offset and the 14% passive respiratory/evaporative dissipation yields the exact net thermal load that must be actively extracted by the Cooling hydraulic loop to maintain thermal equilibrium (Q_{cooling}):

$$Q_{\text{cooling\_nominal}} = M_{\text{Weir}} - 0.10 \cdot M_{\text{Weir}} - 0.14 \cdot M_{\text{Weir}} = 0.76 \cdot M_{\text{Weir}}$$

This nominal 76% distribution factor serves as the primary gain for the predictive feedforward control loop. It represents the precise portion of the user's metabolic rate that will directly cause an over-heating transit if not actively counteracted by the fluid vector.

5.4 Dynamic Sensor-Driven Calculation of Respiratory and Evaporative Fluxes

While static NASA percentage allocations (14%) provide a reliable nominal baseline, a high-fidelity autonomous system must evaluate these fluxes dynamically. By embedding temperature and relative humidity (RH) sensors within the gas loops, the software can abandon static approximations and compute the exact real-time thermal subtraction.

5.4.1 Respiration Heat Loss Calculation

The respiration loop is assessed by monitoring the inlet and outlet states of the helmet ventilation. The software utilizes psychrometric formulations to determine the specific enthalpy (h) of the moist air [J/kg_dry_air] entering and leaving the helmet.

The partial water vapor pressure (p_v) is derived from the Tetens equation for saturation pressure (p_{sat}) [37]:

$$p_{\text{sat}}(T) = 0.61078 \cdot \exp\left(\frac{17.27 \cdot T}{T + 237.3}\right) \quad [\text{kPa}]$$

$$p_v = RH \cdot p_{\text{sat}}(T)$$

Using the total ambient pressure inside the suit (p_{total}), the humidity ratio (ω, mass of water vapor per mass of dry air) is calculated :

$$\omega = 0.622 \cdot \frac{p_v}{p_{\text{total}} - p_v} \quad \left[\text{kg}_{\text{w}}/\text{kg}_{\text{da}}\right]$$

The specific enthalpy (h) is then computed as: [41]

$$h = 1.006 \cdot T + \omega \cdot (2501 + 1.86 \cdot T) \quad \left[\text{kJ/kg}_{\text{da}}\right]$$

By intercepting these values at the helmet inlet and outlet, the total respiratory heat loss (sensible + latent) is calculated directly from the air mass flow rate ($\dot{m}_{\text{air}}$):

$$Q_{\text{respiration}}(t) = \dot{m}_{\text{air}} \cdot \left[h_{\text{helmet\_out}}(t) - h_{\text{helmet\_in}}(t)\right]$$

5.4.2 Torso Perspiration Model

Similarly, the active perspiration heat flux ($Q_{\text{perspiration}}$) within the torso and limb microenvironment is driven by the water vapor pressure gradient between the skin surface and the surrounding air layer trapped beneath the vest.

Using a localized humidity and temperature sensor positioned inside the vest mesh layer ($RH_{\text{suit}}, T_{\text{suit}}$) and a cutaneous temperature sensor (T_{skin}),the software computes the partial vapor pressures:

$$p_{v,\text{suit}}(t) = RH_{\text{suit}}(t) \cdot p_{\text{sat}}\left(T_{\text{suit}}(t)\right)$$

$$p_{v,\text{skin}}(t) = 1.0 \cdot p_{\text{sat}}\left(T_{\text{skin}}(t)\right)$$

The dynamic latent heat flux removed by perspiration is governed by the mass transfer resistance of the garment layers [38]:

$$Q_{\text{perspiration}}(t) = \frac{p_{v,\text{skin}}(t) - p_{v,\text{suit}}(t)}{R_{e,\text{tot}}}$$

where $R_{e,\text{tot}}$ [kPa · m^2/W] represents the total evaporative resistance governing the boundary layer and the garment matrix combined ($R_{e,\text{tot}} = R_{e,\text{a}} + R_{e,\text{cl}}$). While the 205 L/min primary gas ventilation loop actively flushes the helmet cavity to maximize respiratory comfort and CO_2 washout, the air within the torso and limbs microenvironment remains micro-stagnant ($v <$ 0.1 m/s).

For the high-porosity mesh fabric of the active vest, the intrinsic textile resistance is minimal ($R_{e,\mathrm{cl}} \approx 0.002\,\mathrm{kPa \cdot m^2/W}$). However, due to the lack of forced convective currents surrounding the torso, the stagnant air boundary layer exhibits a significantly higher resistance, evaluated according to ISO 9920 standards at $R_{e,\mathrm{a}} \approx 0.035\,\mathrm{kPa \cdot m^2/W}$. This establishes a total torso boundary resistance of $R_{e,\mathrm{tot}} \approx 0.04\,\mathrm{kPa \cdot m^2/W}$.

During high-exertion transits, if the torso air layer becomes fully saturated ($RH_{\mathrm{suit}} \rightarrow 100\%$), $p_{v,\mathrm{suit}}$ approaches $p_{v,\mathrm{skin}}$, causing $Q_{\mathrm{perspiration}}$ to drop toward zero. The control software immediately interprets this as a loss of natural evaporative cooling, automatically forcing the cooling liquid loop to take over the residual thermal load.

5.5 Hydraulic Loop Transient Modelling and Thermal Inertia

The system achieves variable thermoregulation by modulating the mass flow rate ($\dot{m}_{\mathrm{cooling}}(t)$) of water via pump velocity adjustments, while maintaining a constant chiller inlet temperature ($T_{\mathrm{in}} = 2^{\circ}\mathrm{C}$). To accurately control the system during rapid physical transits, the algorithm must account for the fluid's intrinsic thermal mass and transport lag.

Assuming a first-order Lumped Parameter Model for the active garment's hydraulic network, the transient thermal response of the water volume contained within the vest (V_{suit}) is governed by the following ordinary differential equation (ODE) [45]:

$$V_{\mathrm{suit}} \cdot \rho \cdot c_p \cdot \frac{dT_{\mathrm{out}}(t)}{dt} = \dot{m}_{\mathrm{cooling}}(t) \cdot c_p \cdot [T_{\mathrm{in}} - T_{\mathrm{out}}(t)] + Q_{\mathrm{skin}}(t)$$

where ρ is the density of water (1000 kg/m^3), c_p is the specific heat capacity (4186 J/(kg $\cdot{}^{\circ}$ C)), $T_{\mathrm{out}}(t)$ is the time-dependent fluid outlet temperature, and $Q_{\mathrm{skin}}(t)$ is the actual heat flux entering the fluid from the user's body.

For the specific Mesh Vest geometry used in this setup, the internal fluid network incorporates a precise internal volume $V_{\mathrm{suit}} \approx 78$ ml. The total thermal capacity ($C_{\mathrm{hydraulic}}$) of the fluid vector is computed as:

$$C_{\mathrm{hydraulic}} = V_{\mathrm{suit}} \cdot \rho \cdot c_p = (78 \times 10^{-6}\ \mathrm{m^3}) \cdot \left(1000\ \mathrm{kg/m^3}\right) \cdot (4186\ \mathrm{J/kg^{\circ}C}) \approx 326.5\ \mathrm{J/^{\circ}C}$$

This low volumetric capacity ensures a highly reduced thermal mass, allowing the outlet temperature to respond rapidly to changes in pump velocity, which minimizes the transient latency during workload steps.

5.6 Control Loop Strategy: Combined Feedforward-Feedback Architecture

A purely reactive control system (such as a standard closed-loop feedback mechanism) cannot handle the mass transport delay of the system because $T_{\mathrm{out}}(t)$ reacts only after the fluid has completed its circuit through the LCG. To eliminate this transient delay, a combined Feedforward-Feedback control architecture is implemented.

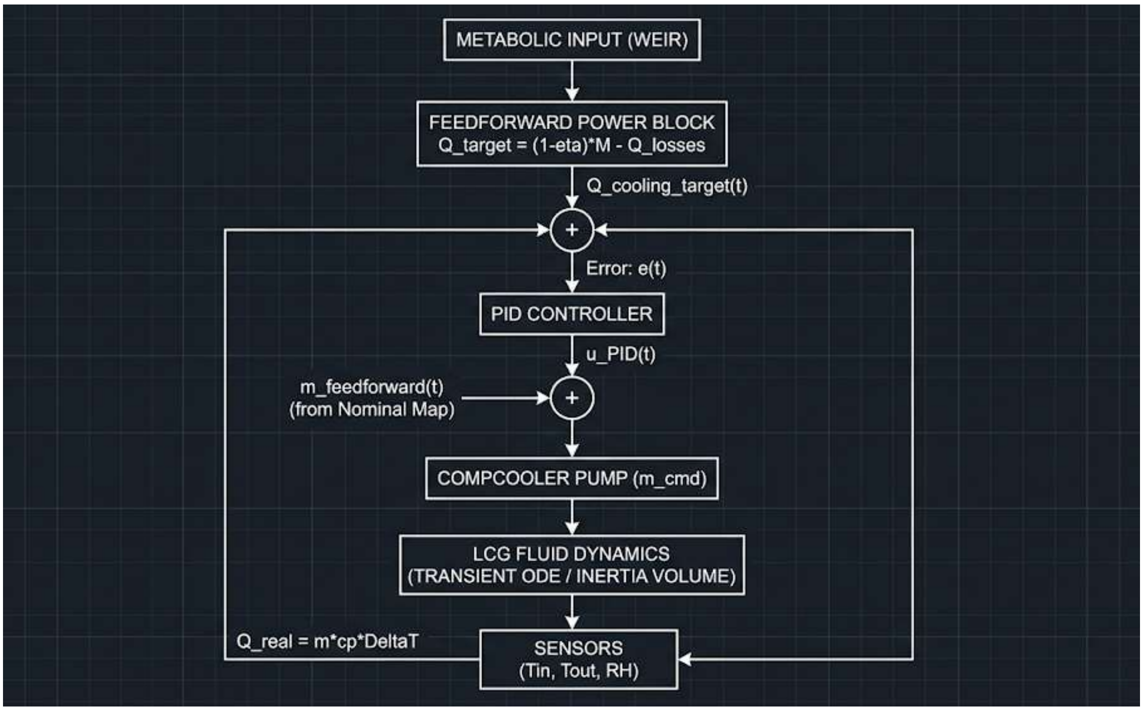

Figure 29 *Metabolic control loop strategy*

5.6.1 Feedforward (Predictive) Power Block with Basal Compensation

The feedforward branch utilizes the instantaneous $M_{\text{Weir}}(t)$ calculation and the sensor-driven loss profiles to compute the predictive net cooling target ($Q_{\text{cooling\_target}}$) that must be absorbed by the liquid loop. To prevent over-cooling during metabolic resting phases, the algorithm implements a baseline resting thermal compensation ($Q_{\text{resting\_compensation}} \approx 75$ W}). This parameter represents the homeostatic heat generation that the human body naturally dissipates via passive radiation and steady-state conduction into the uncooled suit structure at rest, which does not require active fluid refrigeration, that can be obtained more specifically with the Weir formula in resting condition measuring the CO2 expelled by the body.

The predictive mathematical target is formulated as follows:

$$Q_{\text{cooling\_target}}(t) = [(1-\eta)\cdot M_{\text{Weir}}(t)] - Q_{\text{respiration}}(t) - Q_{\text{perspiration}}(t) - Q_{\text{resting\_compensation}}$$

By establishing $Q_{\text{cooling\_target}}(t)$ directly from gas analysis, the software identifies the exact thermal load injected into the suit before it manifests as an elevated skin temperature, allowing the pump driver to proactively adjust its operating speed based on the workload step. If $Q_{\text{cooling\_target}} \leq 0$, the target is capped at zero, and the pump operates at its minimum resting flow rate.

5.6.2 Feedback (PID) Action

In parallel, the Proportional-Integral-Derivative (PID) controller acts as the error-correction mechanism. It monitors the real-time discrepancy (e(t)) between the predictive target and the actual thermal power being extracted by the physical fluid loop:

$$Q_{\text{real}}(t) = \dot{m}_{\text{cooling}}(t)\cdot c_p \cdot [T_{\text{out}}(t) - T_{\text{in}}]$$

$$e(t) = Q_{\text{cooling\_target}}(t) - Q_{\text{real}}(t)$$

The PID algorithm computes its corrective mass flow component as:

$$u_{\text{PID}}(t) = K_p \cdot e(t) + K_i \int_0^t e\,(\tau)d\tau + K_d \cdot \frac{de(t)}{dt}$$

The total commanded mass flow rate ($\dot{m}_{\text{command}}$) sent to the cooling pump driver combines both branches [45,46]:

$$\dot{m}_{\text{command}}(t) = \dot{m}_{\text{feedforward}}(t) + u_{\text{PID}}(t)$$

where $\dot{m}_{\text{feedforward}}(t)$ is derived from a look-up map matching the nominal $Q_{\text{cooling\_target}}$ to steady-state flow requirements. While the feedforward branch handles the instantaneous metabolic transits, the reactive nature of the PID loop compensates for unmodeled system disturbances, environmental losses, and local conduction variations.

5.7 Advanced Framework: Model Predictive Control (MPC) Transition

While the classical combined Feedforward-Feedback architecture provides a reliable baseline for real-time applications, the evolution toward full autonomy in life support systems involves the implementation of a Model Predictive Control (MPC) framework. Unlike the reactive nature of standard controllers, an MPC embeds the explicit ordinary differential equations (ODEs) governing the thermal and hydraulic loop transients directly inside its control law [44].

5.7.1 The Receding Horizon Principle

The MPC controller solves a constrained optimization problem in real time over a finite future time window, termed the *Prediction Horizon* (H_p). At each sampling time step k, the MPC reads the current state vector $x(k) = [T_{\text{out}}(k), T_{\text{skin}}(k)]^T$ and predicts the future thermodynamic trajectory of the suit system up to $k + H_p$.

This predictive projection is driven by the state-space formulation of the hydraulic lumped parameter model described previously. The algorithm minimizes a cost function J defined to maximize astronaut thermal comfort while penalizing excessive pump actuation [44]:

$$J = \sum_{i=1}^{H_p} \left\| T_{\text{out}}(k+i|k) - T_{\text{out\_comfort}} \right\|_Q^2 + \sum_{i=0}^{H_u-1} \| \Delta\dot{m}_{\text{command}}(k+i|k) \|_R^2$$

where $H_u$is the *Control Horizon* ($H_u \leq H_p$), Q and R are weighting matrices that balance control tracking precision against actuator wear, and $\Delta\dot{m}_{\text{command}}$ represents the rate of change of the pump mass flow rate. Following the *Receding Horizon Principle*, the controller computes an optimal sequence of future control inputs over H_u, applies only the first element of this sequence $(\dot{m}_{\text{command}}(k))$, and discards the rest. At the next sampling step k+1, the optimization window shifts forward, new sensor measurements are read, and the calculation is repeated.

5.7.2 Mathematical Handling of State Constraints

The critical advantage of an MPC architecture over conventional PID control is its native ability to compute control actions under hard and soft physical constraints. In the LUNA suit system, the operational envelope of the cooling pump is bounded by physical pump saturation thresholds:

$$\dot{m}_{\text{min}} \leq \dot{m}_{\text{command}}(t) \leq \dot{m}_{\text{max}}$$

Furthermore, the MPC can accept real-time bounds derived from internal environment variables, such as preventing localized chilling that could induce shivering or vasoconstriction by restricting the skin-to-fluid temperature gradients:

$$T_{\text{skin}}(t) - T_{\text{in}} \leq \Delta T_{\text{max\_gradient}}$$

By integrating the Weir metabolic rate (M_{Weir}) as a measured disturbance (feedforward preview), the MPC anticipates workload spikes before they cause changes in the fluid temperature. It initiates pump acceleration in advance, using its internal system model to match the biological transient.

5.8 Bladder Humidity Condensation and Material Mitigation Strategies

Within the operational framework of the LUNA facility testbed, the thermal regulation of the suit mockup utilizes a practical sub-freezing energy storage method. Prior to the simulation transit, the bladder is placed inside a freezer to store baseline thermal capacity.

When the pre-chilled, sub-freezing bladder is integrated into the suit and enters the LUNA analog environment, it encounters a dual thermodynamic boundary condition:

1. **Internal Boundary:** It absorbs the metabolic heat and sweat vapor generated by the astronaut.
2. **External Boundary:** Its sub-zero external surface is exposed to the ambient, higher-temperature atmosphere of the indoor planetary testbed.

Because the testbed room air contains ambient ambient humidity, this massive thermal gradient causes the external surface temperature of the bladder assembly to drop rapidly below the local dew point of the facility atmosphere. Consequently, **instant atmospheric moisture condensation manifests on the exterior-facing side of the bladder envelope**.

Left unmanaged, this exterior condensation introduces a catastrophic risk for the facility: **the irreversible contamination of the simulated lunar regolith analog**. The simulant lunar soil must remain rigorously dry to maintain its mechanical, electrostatic, and geotechnical fidelity. Any water droplets tracking along the suit shell and dripping into the testbed would clump the micro-particles of the regolith, destroying its scientific validity.

To eliminate this threat, the exterior facing of the freezer-chilled bladder must be encapsulated within a specialized multi-functional sleeve that acts simultaneously as a high-efficiency **thermal insulator** and a **capillary moisture absorption matrix**.

5.8.1 Multi-Functional Insulation and Absorption Materials

To prevent external condensation from migrating into the regolith testbed, the sub-freezing bladder core can be jacketed using a combination of technical materials.

A. Closed-Cell Neoprene with Double-Lined Nylon Mesh

The primary structural insulation sleeve is fabricated from high-density, closed-cell **Neoprene (Polychloroprene)** [48].

- **Thermal Insulation:** The closed-cell structure incorporates micro-encapsulated nitrogen gas bubbles, which exhibit an exceptionally low thermal conductivity ($k \approx 0.05$ W/(m · K)). This insulation barrier restricts the rate of heat transfer from the warm room air into the frozen bladder, keeping the outer facing of the sleeve safely above the room's dew point temperature.
- **Moisture Buffering:** The outer facing is double-lined with a brushed nylon technical textile. In the event of extreme transient thermal shocks where minor condensation slips past the thermal barrier, the nylon weave acts as a high-surface-area capillary matrix, trapping liquid water in stable suspension through surface tension and preventing free-standing drops from shedding onto the soil.

B. Silica-Aerogel Infused Polymer Felts

For advanced test profiles requiring prolonged sub-zero cooling capacity without increasing the volumetric thickness of the suit layers, the exterior insulation can be upgraded to **silica-aerogel infused polymer felts** (such as Pyrogel or Cryogel matrixes) [47].

- **Extreme Thermal Confinement:** Silica aerogels possess the lowest thermal conductivity of any known solid ($k \leq 0.015$ W/(m · K)).This allows an ultra-thin ($2 - 3$ mm) sleeve to completely decouple the frozen bladder from the LUNA testbed room atmosphere, ensuring that the outermost boundary layer matches the room temperature exactly, thereby mathematically eliminating the driving force for external condensation.
- **Hydrophobic/Hydrophilic Zoned Protection:** The aerogel matrix is inherently hydrophobic, repelling liquid water completely, while the structural backing felt provides an open pore structure capable of physically arresting any stray moisture via mechanical containment.

C. Hydrophobic 3D Spacer Fabric and Expanded Polyethylene (EPE)

To ensure structural separation of the frozen core, a layer of **3D Spacer Fabric** coupled with thin **Expanded Polyethylene (EPE)** foam is introduced [32].

- **The Air-Gap Buffer Principle:** The 3D spacer fabric utilizes micro-filament pillars to create a highly defined, un-collapsible internal air gap between the sub-freezing bladder wall and the exterior insulation layer. This stagnant air gap acts as an additional insulating boundary layer.

- **Fluid Isolation:** EPE foam is completely non-absorbent and chemically inert. It ensures that even if the frozen bladder undergoes rapid surface frosting during handling, the resulting melt-water is trapped entirely within the internal air-gap compartment, completely isolated from the outer shell of the suit, ensuring 100% dry operations over the planetary simulant testbed.

5.9 Testing campaigns and data

To operationalize the indirect calorimetry framework during extravehicular activity simulations, specific boundary conditions and environmental monitoring protocols were established. In alignment with NASA life support engineering standards, the respiratory quotient (RQ) was set to a constant baseline of 0.85, reflecting a standard mixed-substrate metabolic regimen under nominal operational workloads. By definition, the carbon dioxide production rate ($\dot{V}\mathrm{CO_2}$) was derived from the concentration differential across the closed loop:

$$\dot{V}\mathrm{CO_2} = \dot{V}_{\mathrm{vent}} \cdot \left(C_{\mathrm{CO_2,helmet}} - C_{\mathrm{CO_2,ambient}}\right)$$

where $C_{\mathrm{CO_2,helmet}}$ and $C_{\mathrm{CO_2,ambient}}$ represent the carbon dioxide concentrations monitored at the helmet exhaust port and within the facility testbed environment, respectively. These concurrent concentration streams were logged using a dual-port SENS66 gas analyzer sensor. Utilizing the predefined respiratory quotient, the corresponding oxygen consumption rate ($\dot{V}\mathrm{O_2}$) was calculated analytically via the fixed RQ coupling:

$$\dot{V}\mathrm{O_2} = \frac{\dot{V}\mathrm{CO_2}}{RQ} = \frac{\dot{V}\mathrm{CO_2}}{0.85}$$

The raw energy expenditure (EE) derived from the Weir equation represents the total systemic metabolic output. However, as mentioned in the previous subchapter, physiological heat dissipation occurs through multiple pathways (e.g., respiration, perspiration, and radiation). Thermodynamic baselines dictate that approximately 76% of the total metabolic heat load is transferred via sensible heat conduction to the liquid cooling loop.

Consequently, the calculated energy expenditure was scaled by a factor of 0.76 ($P_{\mathrm{met,\ sensible}} = 0.76 \cdot EE$) to establish a direct, equitable comparison against the active cooling power (P_{cooling})generated across the three discrete mass flow rate levels: High (H), Medium (M), and Low (L).

Figure 30 displays the continuous telemetry profile of the carbon dioxide concentration recorded over time during the executed EVA simulation. As evidenced by Figure 31, the calculated metabolic heat generation curve matches this profile, directly validating the scaling linearity embedded in the simplified Weir formulation. The prominent localized peak observed within the dataset corresponds to a high-exertion phase, specifically when the analog astronaut traversed an inclined crater formation, which induced an elevated physiological workload and a heightened rate of energy expenditure.

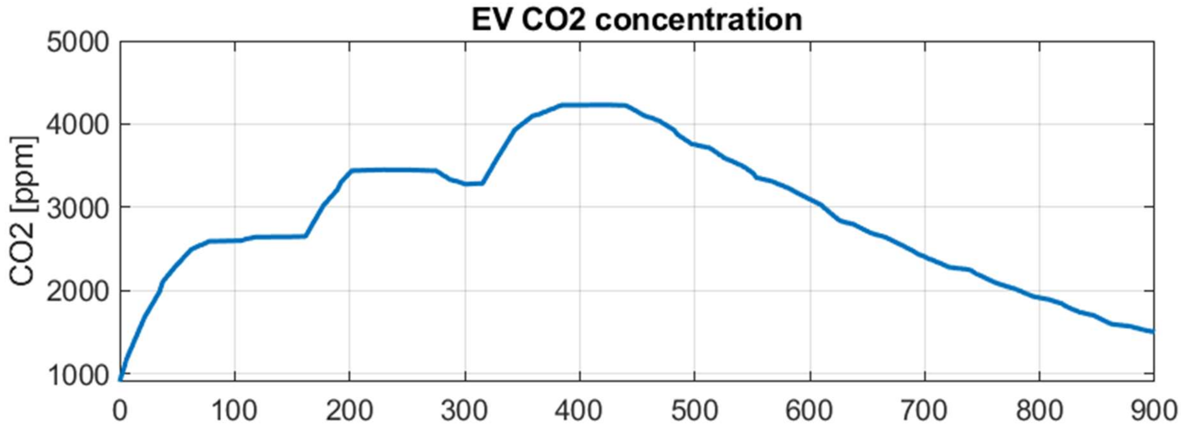

Figure 30 *EV CO2 concentration [ppm] over time [s]*

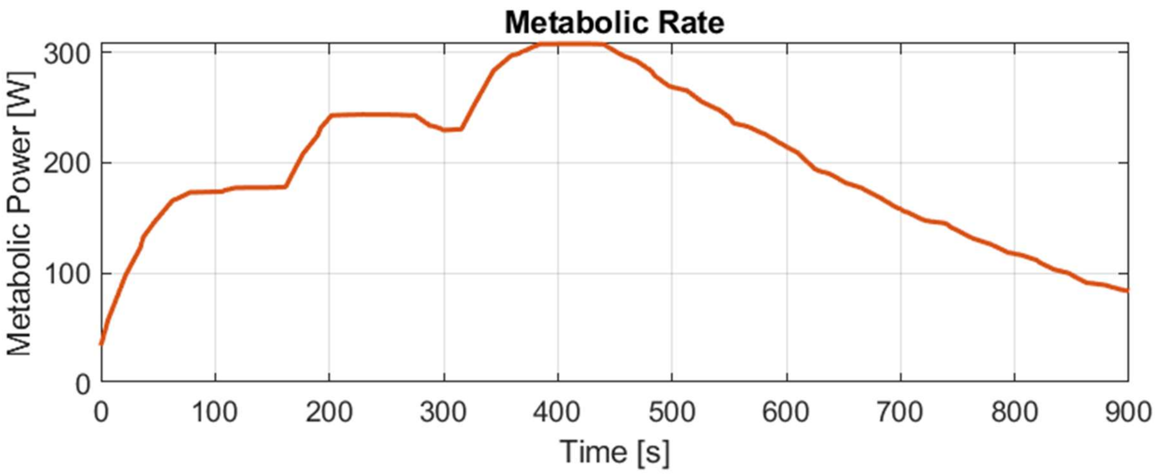

Figure 31 *EV metabolic rate [W] over time [s]*

Figures 32, 33, 34 contrast this transient metabolic heat generation profile against the fluidic cooling power curves sustained by the three designated mass flow rates. Notably, even the maximum operational flow setting (High Level) fails to fully neutralize the absolute peak of the metabolic spike. From an aerospace life support perspective, this localized deficit is acceptable for limited, transient durations, as the structural thermal inertia of the human body safely buffers brief periods of positive heat storage.

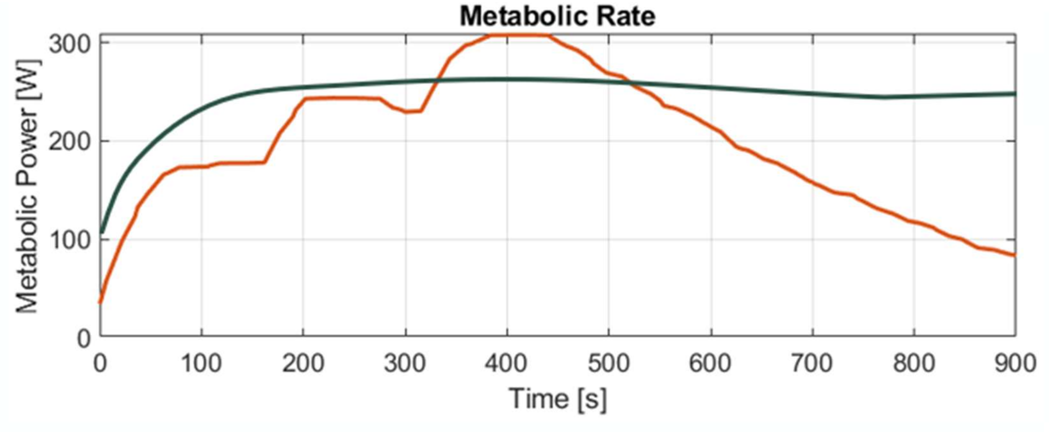

Figure 32 *Comparison between Metabolic Power (red curve) and Cooling power (grey curve) with a mass flow rate of 400 ml/min. Pump level: high.*

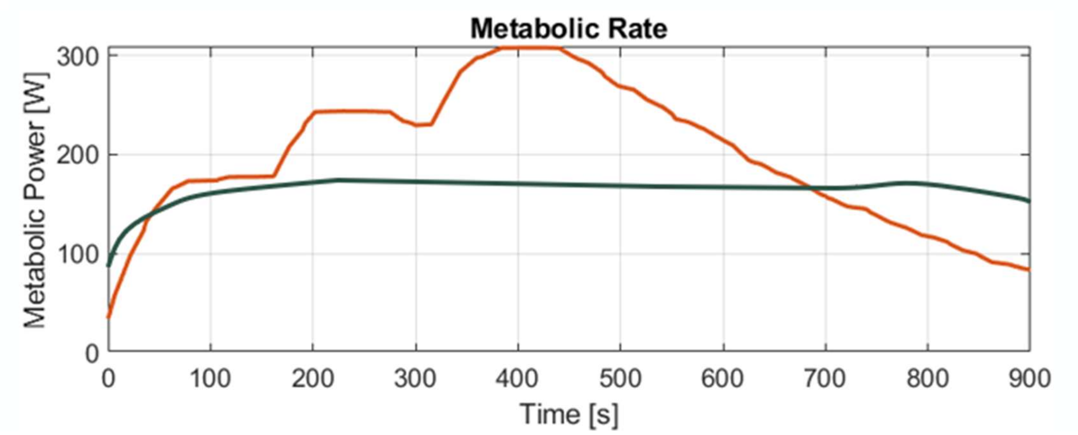

Figure 33 *Comparison between Metabolic Power (red curve) and Cooling power (grey curve) with a mass flow rate of 300 ml/min. Pump level: medium.*

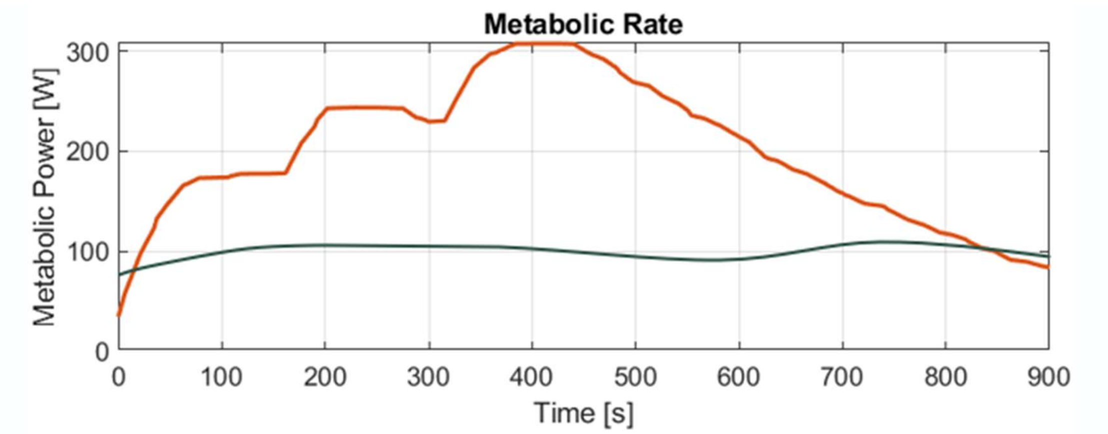

Figure 34 *Comparison between Metabolic Power (red curve) and Cooling power (grey curve) with a mass flow rate of 200 ml/min. Pump level: low.*

To mathematically formalize this tracking performance, a dimensionless cooling efficiency parameter (η_{cool}) is introduced, defined as the ratio of the instantaneous fluidic cooling power to the sensible metabolic heat load:

$$\eta_{\text{cool}}(t) = \frac{P_{\text{cooling}}(t)}{P_{\text{met, sensible}}(t)}$$

This ratio establishes three discrete thermodynamic regimes:

- $\boldsymbol{\eta_{\text{cool}} < 1}$ **(Undercooling):** The metabolic heat generation outpaces the garment heat extraction capacity, causing heat storage within the biological domain.
- $\boldsymbol{\eta_{\text{cool}} > 1}$ **(Overcooling):** The fluidic loop extracts more energy than the body generates, risking localized vasoconstriction and thermal discomfort.
- $\boldsymbol{\eta_{\text{cool}} = 1}$ **(Ideal Thermal Equilibrium):** Represents the nominal target state where the heat generation and extraction rates are balanced.

The primary objective of a closed-loop, autonomous thermal control algorithm is to achieve real-time synchronization where the curves overlap continuously ($\eta_{\text{cool}} \approx 1$). By dynamically modulating the system pump across the discrete cooling levels based on gas-telemetry inputs, the automated controller can proactively counter physical workloads, maximizing astronaut safety and comfort throughout the EVA timeline.

6 Conclusions and future developments

The research presented in this thesis successfully established a comprehensive engineering methodology for the evaluation, thermal study and suit integration of an active thermal control subsystem for simulated extravehicular spacesuit applications. By combining numerical Computational Fluid Dynamics (CFD) campaigns with physical prototyping and hardware integration, this work isolated critical fluid dynamic failure modes and delivered actionable structural mitigations for next-generation Liquid Cooling Garments.

6.1 Key findings

The primary objective of this study was to map the coupled fluidic and thermal degradation profiles of flexible cooling conduits subjected to external mechanical loads. The localized geometric cross-sectional area reduction, modelled as elliptical deformations, revealed a highly non-linear loss of system performance:

- **Moderate Deformation Regime (2 mm restriction):** The system maintains an unconstrained volumetric throughput, preserving approximately 95% of the nominal baseline cooling capacity with satisfactory convective heat transfer rates.
- **Critical Limit-State Boundary (4 mm restriction):** Structural throttling induces a sharp localized velocity spike, and a permanent downstream static pressure drop. Global thermal extraction efficiency drops to the 85% failure threshold, identifying this as the absolute limit of acceptable operational performance.
- **Near-Complete Occlusion Regime (0.5 mm structural clearance, 5.5 mm restriction):** The merging of opposing hydrodynamic boundary layers and an astronomical spike in hydraulic resistance severely choke the mass flow rate. The global heat extraction capacity experiences a catastrophic collapse, dropping to just 29% of the nominal baseline and introducing a severe single-point failure risk.

Because these critical geometric occlusions are induced by localized external loads, such as harnesses or physical kinking at the fluidic interfaces, they cannot be actively compensated for by the software control loop alone.
Additionally, the requirement to often replace the bladder during the activity couldn't be met with the original PLSS due to the necessity of removing the 8 screws to dismount it.

To systematically mitigate these operational hazards, two distinct hardware upgrades were successfully developed, integrated, and validated:

1. **Structural Protection:** Lightweight, high-stiffness Thermoplastic Polyurethane (TPU) protective clips were implemented alongside specialized rigid interface extensions. These components function as mechanical splints, shielding the flexible silicone conduits, maintaining their axial alignment, and guaranteeing a controlled minimum bend radius to prevent structural kinking at the inlet manifold.
2. **PLSS Infrastructure Redesign:** To accommodate the internal routing, electronics, and cooling bladders, a modular, openable Portable Life Support System (PLSS) enclosure was designed and fabricated via additive manufacturing. Sectioned into six distinct modules to

overcome printer volumetric bed constraints, the parts were integrated using form-fitting hexagonal slots engineered to capture structural fasteners securely. The addition of a sliding polymethyl methacrylate (PMMA) lid interface and a dedicated bladder retention bracket decoupled fluid storage from the primary shell, enabling swift subsystem replacement during donning and doffing procedures.

Furthermore, this work successfully validated the integration of real-time respiratory telemetry using a dual-port SENS66 gas analyser connected to a custom-housed Raspberry Pi micro-controller. By implementing the simplified, non-protein Weir equation and scaling it by a factor of 0.76 to account for sensible heat partition, the tracking framework accurately mapped the instantaneous metabolic heat generation. The system successfully captured transient physiological workloads in real time.

6.2 Future developments

To expand upon the foundational engineering framework established in this project, several computational, hardware, and algorithmic milestones are proposed for future iterations:

Sensor Optimization and Instrumentation Upgrades

To further improve the overall system response and ensure the metabolic rate functions as an unconditionally reliable driver parameter, the integration of higher-grade, robust instrumentation is paramount.

- **Gas Telemetry:** Future iterations require the integration of more accurate, robust, and resilient gas sensors, specifically optimized for tight CO_2 and O_2 partial pressure measurements, to eliminate calibration drift during long-duration operations.
- **Thermal Monitoring:** Regarding temperature measurements, the current PT1000 sensors, which were already improved through the physical implementation of a Wheatstone bridge circuit, could potentially be replaced with ultra-precise PT100 probes. This sensor swap would drastically minimize signal noise and maximize thermal measurement accuracy across the skin-garment interface.

High-Fidelity Computational Optimization

To overcome the software element-count and mesh generation limits encountered in this study, future numerical campaigns should leverage High-Performance Computing (HPC) clusters. This will enable full-scale, multi-branch transient conjugate heat transfer simulations. The entire fluidic network can be modelled directly atop a high-fidelity, anthropomorphic human body mannequin, yielding precise, time-dependent spatial distribution data regarding metabolic heat extraction and localized skin temperatures.

Autonomous Closed-Loop AI Control

The empirical tracking performance validated via the Weir formula provides the ideal foundation for an autonomous, predictive thermal regulation loop. Future work will focus on compiling and deploying Machine Learning or closed-loop control algorithms directly onto the embedded Raspberry Pi firmware. By monitoring respiratory gas concentration differentials through the upgraded sensor suite, the intelligent system can achieve proactive thermal tracking with zero thermal lag, modulating pump operating pressures and flow distributions to maintain ideal equilibrium ($\eta_{\text{cool}} = 1$) well before metabolic exertion manifests as physical skin temperature discomfort.

In the framework of the upcoming Artemis lunar missions, this study demonstrates that high-fidelity analog simulation is the ultimate tool to bridge the gap between theoretical engineering and astronaut safety.

Bibliography

[1] NASA. (n.d.). *Artemis Program Official Overview and Mission Milestones*. National Aeronautics and Space Administration. https://www.nasa.gov/specials/artemis/

[2] NASA. (n.d.). *Moon to Mars Architecture: Sustained Lunar Exploration and ISRU Strategies*. National Aeronautics and Space Administration. https://www.nasa.gov/moon-to-mars/

[3] ESA. (n.d.). *The Lunar Gateway: Europe's contribution to cislunar exploration*. European Space Agency. https://www.esa.int/Science_Exploration/Human_and_Robotic_Exploration/Gateway

[4] A. E. M. Casini *et al.*, "LUNA analog facility: Moon simulations in Cologne," in *Proceedings of the German Aerospace Congress (DLRK)*, Stuttgart, Germany, 2023, Document ID: 200873.

[5] A. E. M. Casini *et al.*, "Lunar operations testing in analogue facilities: the ESA-DLR LUNA facility," presented at the *SpaceOps 2022 Workshop*, NASA Ames Research Center, CA, USA, 2022.

[6] A. Zemeny, L. Sardisco, S. Quinteros, *et al.*, "The Luna Analog Facility testbeds (ESA, EAC): contemporary characterization work of highland (lunar) and mare (EAC-1) lunar regolith simulants," *Frontiers in Space Technologies*, vol. 5, art. 1510635, Dec. 2024.

[7] M. N. Newman and J. A. Hoffman, "The evolution of spacesuit technology for extravehicular activity," *Journal of Aerospace Engineering*, vol. 226, no. 4, pp. 341-355, 2015.

[8] H. J. McMann and P. O. Thomas, *US Spacesuits*, 2nd ed. Chichester, UK: Springer Praxis Books, 2012.

[9] NASA, *Extravehicular Mobility Unit (EMU) Systems Data Book*, JSC-66254, NASA Johnson Space Center, Houston, TX, 2017.

[10] G. S. Lutz, *Spacesuit Portable Life Support System Thermal Control Technology Evolution*, NASA Technical Memorandum, TM-2020-220456, 2020.

[11] R. Rhodes, J. Mitchell, and C. West, "Development of the exploration extravehicular mobility unit (xEMU) for Artemis missions," in *Proceedings of the 50th International Conference on Environmental Systems (ICES)*, ICES-2021-124, 2021.

[12] M. Russell, K. Splawn, and S. Thomas, "Axiom Space next-generation planetary spacesuit architecture (AxEMU)," in *IEEE Aerospace Conference Proceedings*, Big Sky, MT, 2024, pp. 1-12.

[13] L. J. West, C. S. Campbell, and T. O'Connell, "Thermal design and analysis of the xEMU spacesuit for lunar south pole exploration," *SAE International Journal of Aerospace*, vol. 15, no. 2, pp. 185-199, 2022.

[14] J. V. Conger *et al.*, "Design and operational testing of modern Liquid Cooling and Ventilation Garments (LCVG)," *Acta Astronautica*, vol. 165, pp. 112-123, 2019.

[15] C. E. Lowrey, "Advanced spacesuit water membrane evaporator for the xEMU portable life support system," in *49th International Conference on Environmental Systems*, ICES-2019-284, 2019.

[16] F. Zhou, M. J. Kim, and S. Park, "Review of personal cooling technologies for terrestrial and high-stress professional applications," *International Journal of Thermal Sciences*, vol. 182, p. 107790, 2022.

[17] J. Smith, A. Martinez, and L. Rossi, "Compact active liquid cooling systems for analog spacesuit simulators and high-workload environments," *Frontiers in Aerospace Engineering*, vol. 3, pp. 45-58, 2024.

[18] K. J. Lynch, M. A. Noyes, and J. R. Marmolejo, "Testing the Exploration ConOps (ExCon) Mockup Suit in Lunar Analog Environments," in *Proceedings of the 52nd International Conference on Environmental Systems (ICES)*, ICES-2023-241, Calgary, Canada, July 2023.

[19] NASA, *Artemis EVA Operations and Support Team Manual*, JSC-67102, NASA Johnson Space Center, Houston, TX, 2022.

[20] M. C. Flores and K. H. Harrison, "Extrication protocols and emergency safety management in rigid analog spacesuits," *Journal of Space Safety Engineering*, vol. 11, no. 1, pp. 85-93, 2024.

[21] COMPCOOLER. *Operational Manual for ICE Water Cooling system* https://www.compcooler.shop/pages/operation-manual-download

[22] T. R. Kuphaldt, *Lessons In Industrial Instrumentation*, 2nd ed. Bellingham, WA: Open Source Textbook Project, 2019.

[23] P. Ripka and A. Tipek, *Modern Sensors Handbook*. London, UK: ISTE Publishing, 2007.

[24] J. G. Webster, *The Measurement, Instrumentation, and Sensors Handbook*. Boca Raton, FL: CRC Press, 2014.

[25] Interlink Electronics, *Force Sensitive Resistor (FSR) Integration Guide and Technical Specifications*, Camarillo, CA, 2021.

[26] J. A. Szweda, *Polymer Thick Film Technology*. Oxford, UK: Elsevier Advanced Technology, 2011.

[27] Sensirion AG, *SEN6x Environmental Node Gas and Particulate Matter Sensor Datasheet*, Stäfa, Switzerland, 2023.

[28] A. Oprea, N. Barsan, and U. Weimar, "Metal oxide semiconductor gas sensors: Signal conditioning and interfacing," *Sensors and Actuators B: Chemical*, vol. 121, no. 2, pp. 624-635, 2007.

[29] F. M. White, *Fluid Mechanics*, 8th ed. New York, NY: McGraw-Hill Education, 2016.

[30] T. L. Bergman, A. S. Lavine, F. P. Incropera, and D. P. DeWitt, *Fundamentals of Heat and Mass Transfer*, 7th ed. Hoboken, NJ: John Wiley & Sons, 2011.

[31] E. H. Wissler, "A review of Pennes' bioheat equation and its application to modeling human thermal regulation," *Journal of Applied Physiology*, vol. 85, no. 1, pp. 35-41, 1998.

[32] J. E. Mark, *Polymer Data Handbook*, 2nd ed. Oxford, UK: Oxford University Press, 2009.

[33] M. G. Levitzky, *Pulmonary Physiology*, 9th ed. New York, NY: McGraw-Hill Education, 2018.

[34] J. B. de V. Weir, "New methods for calculating metabolic rate with special reference to protein metabolism," *The Journal of Physiology*, vol. 109, no. 1-2, pp. 1-9, 1949.

[35] J. A. McLean and G. Tobin, *Animal and Human Calorimetry*. Cambridge, UK: Cambridge University Press, 2007.

[36] P. Webb, "The physiology of heat regulation in spacesuits," *Aviation, Space, and Environmental Medicine*, vol. 58, pp. 115-121, 1987.

[37] O. Tetens, "Über einige meteorologische Begriffe," *Zeitschrift für Geophysik*, vol. 6, pp. 297-309, 1930.

[38] A. P. Gagge, "A psychrometric chart for human body heat and thermal comfort," *ASHRAE Transactions*, vol. 72, pp. 256-274, 1966.

[39] International Organization for Standardization, *Ergonomics of the thermal environment — Estimation of the thermal insulation and water vapour resistance of a clothing ensemble*, ISO Standard 9920:2007, 2007.

[40] J. A. J. Stolwijk, *A mathematical model of physiological temperature regulation in man*, NASA CR-1855, NASA, Washington, DC, 1971.

[41] ASHRAE, *ASHRAE Handbook—Fundamentals*. Atlanta, GA: American Society of Heating, Refrigerating and Air-Conditioning Engineers, 2021.

[42] NASA, *Human Integration Design Handbook (HIDH)*, NASA-SP-2010-3407, Office of the Chief Health and Medical Officer, Washington, DC, 2014.

[43] NASA, *Space Flight Human-System Standard: Volume 2: Human Factors, Habitability, and Environmental Health*, NASA-STD-3001, OCHMO, Houston, TX, Revisions 2022/2023.

[44] E. F. Camacho and C. Bordons, *Model Predictive Control*, 2nd ed. London, UK: Springer-Verlag, 2007.

[45] K. J. Åström and T. Hägglund, *Advanced PID Control*. Research Triangle Park, NC: International Society of Automation (ISA), 2006.

[46] NASA, *Spacecraft Thermal Control Handbook*, Aerospace Press, El Segundo, CA, 2020.

[47] J. Fricke and A. Emmerling, "Aerogels—Preparation, properties, applications," *Journal of the American Ceramic Society*, vol. 75, no. 8, pp. 2027-2035, 1992.

[48] L. Goldstein and M. N.集中, "Thermal conductivity and condensation insulation parameters of closed-cell polychloroprene foams," *Journal of Applied Polymer Science*, vol. 114, no. 3, pp. 1422-1431, 2009.